A STUDY OF WATER CROSSOVER IN POLYMER ELECTROLYTE MEMBRANE FUEL CELLS

by

Tak Cheung Yau

B.Eng., Hong Kong University of Science and Technology, 2004

A THESIS SUBMITTED IN PARTIAL FULFILLMENT OF THE
REQUIREMENTS FOR THE DEGREE OF
MASTER OF APPLIED SCIENCE

in

The Faculty of Graduate Studies
(Chemical and Biological Engineering)

THE UNIVERSITY OF BRITISH COLUMBIA
(Vancouver)
January 2011

Abstract

Water crossover between anode and cathode of polymer electrolyte membrane fuel cells has been studied together with fuel cell performance at steady state. The parameters considered included temperature, pressure, inlet humidity and the presence of a cathode microporous layer. In general water crossover was found to be increasingly toward the anode side with increasing current density up to a certain point beyond which a plateau was observed. Larger cathode-to-anode inlet humidity gradient, lower temperature and higher cathode pressure enhanced water crossover to the anode, due to a higher downstream humidity at the cathode catalyst layer.

The presence of a cathode microporous layer enhanced water crossover to the anode only when the cathode inlet humidity was low. It was proposed that this layer imposed a larger diffusion barrier between the cathode channel and the membrane interface whose effects diminished at high relative humidity. The zero crossover rate under zero humidity gradients with no load regardless of the presence of the cathode microporous layer suggested that capillary action was not a contributing factor for the action of the layer.

In addition, the quantitative data obtained by the water crossover measurement equipment were found to be useful in model validation and parameter estimations. The data could pinpoint inadequacies in models, as well as providing estimated parameters that were more consistent with changes in the oxygen concentration and fitted better to both the current density and water crossover data given a certain voltage.

Preface

This thesis contains materials that have been published or in press.

Section 1.6 is an excerpt of Chapter 8 in *Handbook of PEM Fuel Cell Durability Volume 2: PEM Fuel Cell Diagnostic Tools*, to be published by CRC Press in 2011. The author of this thesis was the principle author of all text in the aforementioned section, with minor editing by other authors of the published work namely Dr Xiaotao Bi, Dr Jürgen Stumper and Pierre Sauriol.

Section 2.4, chapter 3 and chapter 5 were published in *Journal of the Electrochemical Society* volume 157 page B1310-B1320 in 2010. The experimental data presented in chapter 3 were obtained by Pierre Sauriol. The author of this thesis was the principal contributor in data analysis and the principal author of all text in the aforementioned sections, with minor editing and advice by other authors of the published work namely Dr Xiaotao Bi, Dr Jürgen Stumper and Pierre Sauriol.

Table of Contents

List of Tables

List of Figures

Nomenclature

Symbols

a	1200 $molm^{-3}$	Sulfonic group concentration
A	cm^2	Cell active area
c		Dimensionless concentration
c'		Intercept of calibration line
C	$molm^{-3}$	Reactant concentration
d	m^2s^{-1}	Diffusivity
D	m^2s^{-1}	Effective diffusivity
E_0	V	Open circuit potential
F	96500 $Cmol^{-1}$	Faraday's constant
I	Acm^{-2}	Local current density
$\bar{I}$	Acm^{-2}	Average current density
$i_{o,c}$	$mAcm^{-2}$	Exchange current density
J	$molcm^{-2}s^{-1}$	Molar flux
$\bar{J}$	$molcm^{-2}s^{-1}$	Average molar flux
L	m	Thickness (for subscripts *G*, *m*, *M*)
L_c	m	Channel length
L_w	m	Channel width
m'		Slope of calibration line
n_C		Number of electrons in electrochemical reaction
$\dot{n}$	$mols^{-1}$	Molar flow rate
N		Number of fitting points for one response
N_c		Number of channels
P	kPa	Partial Pressure
r	m	Pore radius
R	8.314 $Jmol^{-1}K^{-1}$	Universal gas constant
R_{elec}	Ω	Electrical resistance
RH		Relative humidity
T	K	Temperature
U	V	Cell voltage
V_m	m^3mol^{-1}	Molar volume
x	m	Distance along channel
y		Mole fraction (wet basis)
y'		Mole fraction (wet basis)

Greek letters

α		Water crossover coefficient
α_C		Kinetic transfer coefficient
γ	ms^{-1}	Membrane interfacial water transfer coefficient

δ	$molA^{-1}m^{-1}$	Oxygen diffusivity factor
η	V	Overpotential
ψ	$molm^{-1}s^{-1}Pa^{-1}$	Permeability
σ	$cm^{2}\Omega^{-1}$	Effective membrane conductivity
σ'	$cm^{2}\Omega^{-1}$	Membrane conductivity
τ	Nm^{-1}	Surface tension

Subscripts

$+$	Proton
act	Activation
A	Anode
bwd	Backward reaction
cal	Calibration
C	Cathode
cc	Cathode catalyst layer to channel
CL	Catalyst layer
desorption	Desorption
eqm	Equilibrium
experimental	Experimental
fs	Free surface
fwd	Forward reaction
G	GDL
H_2	Hydrogen
H_2O	Water
in	Inlet
m	Membrane
M	MPL
MFC	Mass flow controller for fuel cell feed
MFM	Mass flow meter for dilution gas
model	Model prediction
ohm	Ohmic
out	Outlet
O_2	Oxygen
ref	Reference conditions
sat	Saturation
total	All gases
X	Crossover (anode to cathode)

Abbreviations

CAM	Capillary action model
CDF	Current density only fitting method
DRF	Dual response (current density and water

	crossover) fitting method
EOD	Electro-osmotic drag
GC	Gas chromatography
GDL	Gas diffusion layer
MEA	Membrane electrode assembly
MPL	Microporous layer
PEMFC	Polymer electrolyte membrane fuel cell
RH	Relative humidity
SSR	Sum of squared residuals
TRM	Transport reduction model

Acknowledgments

I would like to take this opportunity to thank my supervisor Prof. Xiaotao Bi from the Department of Chemical and Biological Engineering at UBC and Dr Jürgen Stumper from the Automotive Fuel Cell Cooperation Corporation (AFCC). They made this research project possible by applying for grants and allocating other required resources. During the course of my study, they have been providing valuable guidance and comments so that my work could be headed to the way it is now. I also appreciate their patience especially at the early stages. Also I thank NSERC and AFCC for funding the project.

I have always been helped by a lot of friendly colleagues. First I want to mention Mr. Pierre Sauriol, a pioneer of the water crossover measurement project. Although he left the research group long before I started my study, he generously answered all of my questions in his own free time to put me on track. The Lab Equipment Development and Service team at AFCC, especially Mr. Tan Uong, tried their best to construct the setup to my specifications. Prof. David Wilkinson and current UBC research teammates Dr. Lifeng Zhang, Mr. Ryan Anderson and Mr. Yulong Ding have made a lot of useful discussions with me, as well as Dr. Max Cimenti and Mr. Mickey Tam at AFCC. I gained technical knowledge, workplace experience as well as friendship from all these guys.

Other friends, both old and new, have been supportive during my stay in Vancouver. Credits first go to another student at the department Mr. Wilson Lam, whom I met when I was a freshman in 2001 and encouraged me to take on a new challenge of studying on the other side of the globe. He and his girlfriend Ms. Fiona Lau made my days enjoyable. Also Dr. Tommy Cheng and Mr. Homan Liu showed their sincerity towards their new friendship with me which I really appreciate.

Finally, my study is backed unconditionally by my parents and my sister in Hong Kong. They are the ones who removed all my obstacles and pushed me forward when I lacked energy, without a single complaint of my lack of accompany. I am proud to receive their love and care and I hope that what I have achieved can make them proud in return.

To my grandmother whom I failed to accompany during her last stages of life.

1. Introduction

Fuel cells are strong candidates for the next generation electric power generators. Compared to current combustion based technologies, fuel cells generate electricity in a single step without moving parts, and are therefore much simpler (Barbir 2005). In addition, the maximum efficiency of a hydrogen fuel cell to produce electricity can exceed that of a Carnot engine at temperatures at less than 800 °C (Larminie and Dicks, 2003). Compared to batteries, fuel cells can be recharged much quickly by means of refuelling (O'Hayre et al. 2006). For automobiles, the use of hydrogen fuel eliminates the emission of carbon monoxide, hydrocarbons, nitrogen oxides and sulphuric oxides locally; because of the only product of the fuel is water:

$$2H_2 + O_2 \rightarrow 2H_2O \qquad [1]$$

This thesis focuses on one type of fuel cells called polymer electrolyte membrane fuel cells (PEMFCs). One special advantage of PEMFCs is that they are highly scalable from cell phone applications to powering buses. Also, using a polymeric electrolyte with no corrosive hazards, PEMFCs are safe to operate in automotives compared to alkaline fuel cells (Larminie and Dicks, 2003). Combining all the above advantages, it would be of good practical interest to improve the performance of PEMFCs. To develop high performance PEMFCs, water management has been regarded as a vital topic in this technology (Larminie and Dicks, 2003).

This first chapter is an introduction to the importance of water management (and water crossover in particular) in PEMFCs and previous research efforts, which leads to the establishment of the research goals of this thesis project. This would be followed by the experimental and methodology section, which discusses in detail the equipment, test protocol and the mechanistic model used in this project. The experimental results and discussion of proposed studies would be presented in the following research chapters. Chapter 5 presents a numerical study using the said model before the thesis is concluded.

1.1. Components in a PEMFC

A single cell contains anode and cathode sides, separated by the membrane electrode assembly. The reactants are brought to the cell through the channels in flow field plates. They then diffuse to the catalytic sites through a porous diffusion media and then undergo electrochemical reactions and give rise to a current. At the anode hydrogen is oxidized to give protons and electrons:

$$H_2 \rightarrow 2H^+ + 2e^- \qquad [2]$$

The protons travel through the electrolyte membrane to the cathode side, and the electrons travel through the anode porous diffusion media and the conductive flow field plate to the external circuit in which work is extracted from the electrons. The electrons go back to the cell to complete the circuit through cathode flow field and porous diffusion media to the catalytic sites and combining with oxygen, and the protons travel through the membrane to give water as a product:

$$\frac{1}{2}O_2 + 2H^+ + 2e^- \rightarrow H_2O \qquad [3]$$

The above two reactions have to be catalyzed. In PEMFCs, platinum is the most common catalyst due to its high catalytic activity. The porous diffusion media and the flow field plates have to be electrically conductive with minimal resistance along the pathway of the electrons. The common choices of materials are carbon paper or carbon cloth for the porous media, and graphite for the flow field plates.

For the polymer electrolyte membrane, the most common choice is perfluorosulfonic acid membranes and one example is Nafion. The structure of the polymer is given in Figure 1.

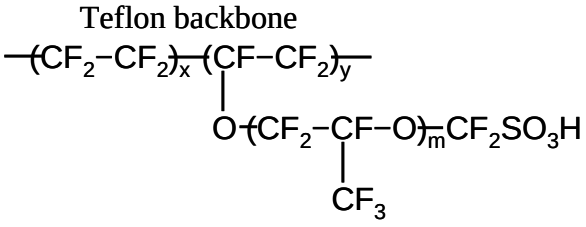

Figure 1. Chemical structure of Nafion.

The Teflon backbone provided mechanical strength to the membrane. The ionic sulfonic groups provide charged sites to accommodate proton transport. Also due to the hydrophilic nature of the sulfonic groups, water is readily absorbed into the polymer matrix. This absorbed water forms hydrophilic channels surrounded by hydrophobic Teflon backbones. This is illustrated in Figure 2. As explained later, the absorbed water also helped facilitate proton conduction in the membrane. The complex relationship between Nafion and water implies the importance of water management in PEMFCs.

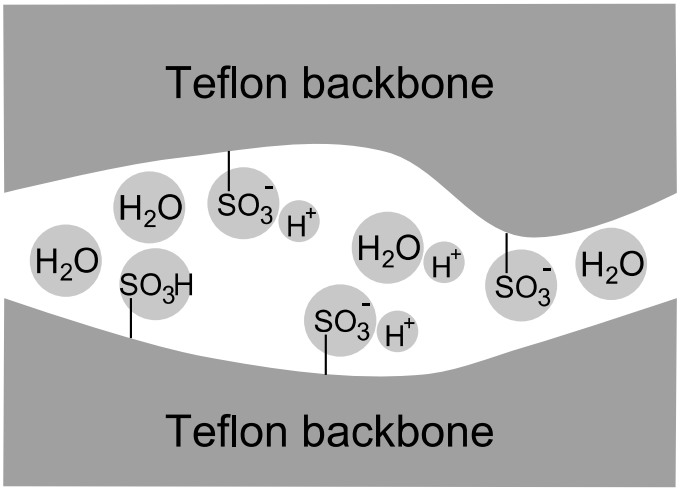

Figure 2. Water channels in Nafion provide proton transport within a hydrophobic Teflon backbone.

1.2. Losses in a Fuel Cell and Water Management

Under a current load, the fuel cell will experience three types of losses which cause a lower voltage compared to the open circuit situation.

To draw a current one has to depart from the equilibrium situation. This departure would lead to a voltage loss (activation overpotential η_{act}). The resulting current density, which is the difference between current densities from forward and backward reactions, is described by the Butler- Volmer equation for a first order reaction (O'Hayre et al. 2006)

$$I = i_{fwd} - i_{bwd} = i_{o,c}\frac{C}{C_{ref}}\exp\left(\frac{\alpha_c n_c F \eta_{act}}{RT}\right) - i_{o,c}\frac{C}{C_{ref}}\exp\left(-\frac{(1-\alpha_c) n_c F \eta_{act}}{RT}\right) \quad [4]$$

The Butler-Volmer equation could not be solved explicitly for η_{act}, but for normal situations in fuel cells the backward reaction could be ignored due to a large value of η_{act}. This approximation results in the Tafel equation

$$\eta_{act} = -\frac{RT}{\alpha_c n_c F}\ln\left(i_{o,c}\frac{C}{C_{ref}}\right) + \frac{RT}{\alpha_c n_c F}\ln I \quad [5]$$

Diffusional resistance of reactants to the reaction sites will greatly increase the first term in the Tafel equation and hence η_{act} through a small value of C. This is called concentration polarization.

The protons generated from the anodic reaction have to travel to the cathode to complete the circuit. In addition, electron transfer from the anode sites to the cathode sites also encounters electrical resistances, e.g. resistance of the conductors and contact resistances. These charge transfer processes obeys Ohm's law.

$$\eta_{ohm} = I\left(R_{elec} + \frac{L_m}{A\sigma'}\right) \quad [6]$$

Incorporating these losses, the overall voltage- current relationship is given by

$$U = E_0 - \eta_{act,A} - \eta_{act,C} - \eta_{ohm}$$
$$= E_0 - \frac{RT}{\alpha_{c,A} n_{c,A} F}\left(\ln I - \ln\left(i_{o,c,A}\frac{C_{H_2}}{C_{H_2,ref}}\right)\right) - \frac{RT}{\alpha_{c,C} n_{c,C} F}\left(\ln I - \ln\left(i_{o,c,A}\frac{C_{O_2}}{C_{O_2,ref}}\right)\right) - I\left(R_{elec} + \frac{L_m}{A\sigma'}\right) \quad [7]$$

Now we can examine the effects of water on fuel cell performance. The membrane conductivity σ'^{-1} increases with water content (Zawodzinski et al. 1993a, b). If the water content in the membrane is too low, σ'^{-1} and hence cell performance can be adversely affected. On the other hand, when the water produced from the cell reaction at the cathode cannot be removed efficiently, water fills up the pores in the electrode blocking access of oxygen to the cathode catalyst and decreasing C_{O_2}. This is referred to as flooding of the electrode. Two of the three loss mechanisms are related to water in a PEMFC. Therefore, water management has been an important issue in the operation of the PEMFCs (Murahashi et al. 2006, Lu et al. 2007).

A useful parameter to study in this context is the water crossover flux, which is defined as the flux of water transported through the membrane. In the literature there are different sign conventions, but here we define the flow of water from the anode to the cathode as positive. A closely related parameter, the water crossover coefficient α, is defined as the water crossover rate divided by the rate of water generation from electrochemical reactions (Sauriol et al. 2009). Understanding how the water is transferred in a fuel cell can provide insights in proper water management to avoid flooding and dry-out conditions.

1.3. Modes of Transfer in PEMFCs

There are several modes of water transfer from one side to the other in PEMFCs. Within the channels, there is a significant flow of gases. This motion moves species to the direction of flow by means of convection (O'Hayre et al. 2006). Through the GDL, MPL and the catalyst layer, diffusion and Darcy's flow through capillary pressure govern water transfer in vapour and liquid forms respectively. On the other hand, reactant gases (hydrogen and oxygen) move to the reaction site by diffusion. It has been suggested that

the transport of gases through the catalyst layer is governed by Knudsen diffusion (Stumper et al. 2005), which is independent on the overall pressure.

Under a current load, protons generated at the anode catalyst layer move to the cathode catalyst layer under potential and concentration gradients. Within the membrane there are three mechanisms for proton transfer: surface hopping mechanism, Grotthus mechanism and vehicle mechanism (Choi et al. 2005). In surface hopping mechanism, protons 'hop' from one sulfonic group to another within the hydrophilic channel of the membrane by losing bonding to one sulfonic group and forming with the other. Grotthus mechanism is a similar action to proton hopping, except the protons hop from one water molecule in the bulk to another. As suggested by the name, vehicle mechanism means the protons are hydrated to form hydronium (H_3O^+) or Zundel ion ($H_5O_2^+$) etc., and travel en masse to the cathode side. This action would lead to water transport from the anode side to the cathode side of the membrane, and this mechanism of water transport is called electro-osmotic drag (EOD). The EOD coefficient is defined by the number of water molecules dragged to the cathode side per proton produced. A mix of these mechanisms can occur together in a polymer electrolyte membrane.

In the polymer electrolyte membrane, water can diffuse from one side to the other due to concentration gradients. It can also be viewed that water travels through the channels inside membrane through hydraulic pressure gradients. This is called hydraulic permeation (Barbir 2005). The differences between these two models are reviewed in Wijmans and Baker (1995) and the authors favoured the solution- diffusion model for membrane transport. At the membrane interface, Springer et al. (1991) proposed an equilibrium relationship between the water vapour (or liquid water) and the membrane surface. The alternate theory is there is a dynamic absorption and desorption process governing water transport, in which the driving force is the difference between the water content at the membrane interface and the equilibrium water content with the vapour/ liquid phase (Berg et al. 2004, Ge et al. 2005, Monroe et al. 2008).

1.4. Measurements of Water Transfer Related Membrane Properties

A series of papers from Zawodzinski et al. presented ex-situ data for Nafion and other poly(perfluorosulfonic acid) membranes. They include water uptake, self diffusion coefficients and conductivity (1993a, 1993b), and EOD coefficients (1993b, 1995). In those experiments the membranes were directly exposed to liquid water or water vapour with various activities. Self diffusion coefficients and conductivity were found to increase by increasing the water content, while the EOD coefficient stayed relatively constant with 1 mole of water dragged per mole of proton over a broad range of water contents. The equilibrium water content of the membrane increased with the water vapour activity to which the membrane was exposed. They developed an empirical relationship at 30 ˚C, as reported in Springer et al. (1991):

$$c_{H_2O} = 0.043 + 17.81RH - 39.85RH^2 + 36.0RH^3 \qquad [8]$$

One thing to note is that even at 100% humidity, the equilibrium water content in the membrane was significantly less than that in contact with liquid water. Since water vapour at 100% humidity is in equilibrium with liquid water, the discrepancy in water content was not consistent with the zeroth law of thermodynamics. This is called the Schroeder's paradox and it has been suggested that it is due to the thermal history of the membranes under concern and experimentally it is possible to eliminate the discrepancy if the membranes underwent the same heat treatment before each liquid and vapour equilibrium test (Onishi et al. 2007).

Majsztrik et al. (2007) determined steady state water permeation rates across the membrane by placing them between two chambers. From a mass transport model, they found that the overall transport of water through the membrane was limited by interfacial transport which could be explained by the Teflon rich surface layer. Using a similar setup, Monroe et al. (2008) found that interfacial limitations in water transport would be dominant when the membrane thickness was less than 300 μm.

The following paragraphs introduce similar studies using in-situ setups in the literature, which involve measuring water transfer across the membrane in an MEA sandwiched between flow field plates like in a normal fuel cell.

Motupally et al. (2000) measured water transfer from liquid water filled channels on one side and dry nitrogen fed channels on the other. Their results demonstrated the correlation between literature reported self-diffusion coefficients and Fickian diffusion in Nafion membranes obtained by nuclear magnetic resonance spectroscopy (Zawodzinski et al. 1991). Ge et al. (2005) developed mass transfer models and determined diffusion and absorption and desorption coefficients from curve fitting in-situ diffusion data for Nafion membranes.

Husar et al. (2008) isolated the effect of hydraulic pressure by feeding liquid water with different pressure through anode and cathode channels. When measuring vapour phase diffusion, the gas pressures were kept the same for anode and cathode to eliminate pressure effects, while electro-osmotic drag was eliminated by simply applying zero current density. An over-saturated wet side and unhumidified dry side were used to maximize diffusion gradients to determine the diffusion coefficient of water. The electro-osmotic drag was isolated in a running fuel cell by feeding fully humidified gas streams at the same pressure, therefore eliminating diffusion and hydraulic permeation effects. They found that hydraulic permeation yielded crossover flux at least one order of magnitude lower than back diffusion and EOD. Diffusion coefficients increased with temperature and decreased with pressure. They obtained EOD coefficients increasing with current density and temperature, ranging from 0.3 at 40 °C and 0.3 Acm^{-2} to 1.1 at 60 °C and 1 Acm^{-2}.

An alternative method to measure electro-osmotic drag coefficient is to feed hydrogen to both anode and cathode channels, and a current is withdrawn by applying a potential difference across the electrodes (Ye and Wang 2007a). This 'hydrogen pump' technique oxidizes hydrogen to produce protons at the anode, while protons are reduced at the cathode side. Thick membranes (200 μm) were used and the same inlet relative humidities at both sides of the membrane were set to minimize the rate of diffusion due to

humidity gradients. They obtained an EOD coefficient of 1.07 from 40% to 95% inlet RH for Gore membranes. Ge et al. (2006) performed similar experiments on Nafion membranes and found that EOD coefficient increased with membrane water content and temperature, but was insensitive to current density. Braff and Mittelsteadt (2008) used dead ended anodes to minimize the humidity gradients along the channel. They searched for the feed ratio between water and hydrogen required for a metastable operation between dryout and flooding, with that ratio corresponding to the electro-osmotic drag coefficient. They found that the EOD coefficient decreased below unity under low RH conditions and suggested a hopping mechanism for proton transfer under those conditions.

Kim and Mench (2009) used anode and cathode flow field plates with different coolant temperatures to apply a temperature gradient across the membrane, and found that water was transported from the cold side to the hot side of the membrane. This transfer rate increased by increasing the temperature gradient as well as the average temperature of the two sides of the membrane.

1.5. Measurement of Water Crossover

To represent water crossover, in some articles α is referred to as the net electro osmotic drag coefficient, which is the water transfer rate divided by the proton generation rate. Shall we denote this quantity by β, we have

$$\beta = \frac{\alpha}{2} \qquad [9]$$

where α is what was defined previously in this thesis.

Effects of Operating Conditions

There is an abundance of results in the literature on the effect of operating conditions on water transfer. An early work by Choi et al. (2000) reported that when the current density was increased, β decreased. For humidified cathode this trend ceased at current densities greater than 0.2 Acm^{-2}. Also by a mass balance on the non-humidified cathode side they observed a decrease in water flow into the membrane as the current density increased.

Janssen and Overvelde (2001) showed that using dry anodes, β could be negative for counter-current gas flows. This meant that the diffusion of water from cathode to anode dominated over the electro-osmotic drag. Other groups had reported a decrease in β upon an increase in current density (Murahashi et al. 2006, Atiyeh et al. 2007, Yan et al. 2006).

When the hydrogen stoichiometry changed from 1.5 to 4, Janssen and Overvelde (2001) found that β did not respond differently. Colinart et al. (2009) found that water crossover to the anode side increased with dry hydrogen flow rate rather than stoichiometry. On the cathode side, β was insensitive to both stoichiometry and flow rate.

Various researchers studied the effect of inlet relative humidity on water transfer. In general, higher inlet humidity at the cathode side decreased β and also the anode-to-cathode water transfer factor, while higher anode inlet humidity would do the reverse (Colinart et al. 2009). This is a direct consequence of the water concentration gradient between the two sides of the membrane. Net electro-osmotic drag coefficient β also decreased with increasing cathode pressure (Yan et al. 2006). It has been explained that a higher cathode pressure increased the humidity for the same water vapour mole fraction (Yan et al. 2006). While a lower cell temperature would lead to the same effect, increasing cell temperature would lead to a higher value in β (Colinart et al. 2009).

Effects of MEA Construction

Janssen and Overvelde (2001) briefly studied the effect of membranes on water crossover. They used Nafion 112 and Nafion 105 in their experiments and reported that the thinner Nafion 112 yielded a smaller value in β under the same condition. It was probably due to the enhanced back diffusion using thinner membranes which led to higher concentration gradients, despite a lower sulfonic group density in Nafion 112.

Atiyeh et al. (2007) experimentally measured the water transfer factor from MEAs with and without microporous layers. They found that the addition of a microporous layer at the cathode did not change the overall water transfer significantly. The same results were obtained by Janssen and Overvelde (2001) at a current density of 0.4 Acm^{-2}. When the current density was 0.6 Acm^{-2}, the difference was more pronounced, regardless of

humidification conditions. The water transfer was found to be less if microporous layers were applied. Kim et al. (2010) found that water crossover was more to the cathode side when an MPL was added to both anode and cathode compared to adding MPL to the cathode side only. While keeping the cathode channel saturated they varied the anode channel and produced consistent results. When there were no MPL on both sides, the water crossover coefficients were the highest. Dai et al. (2009) used water filled anode and a dry air cathode channel to measure water transfer to the cathode channel through the GDL. They found that the addition of a microporous layer could reduce water transfer to the cathode channel at dry air flow rates greater than 7.44×10^{-4} $mols^{-1}$. The authors claimed that at higher air flow rates more water was driven out of the membrane, which caused a higher capillary pressure in micropores and hence decreased the transport efficiency through the GDL. Murahashi et al. (2006) used hydrophobic microporous layers in both anode and cathode. Although they did not study directly the effects of the layer on water transfer, they found that when capillary pressure was included in their calculations, a lower overestimate in β was observed. They claimed that capillary action increased the activity of water vapour at the membrane interface which in turn increased electro-osmotic drag and back diffusion coefficients and decreased water transfer from anode to cathode.

Ye and Wang (2007b) found that if the diffusivity through GDL was better, the net water transport from anode to cathode was larger, in addition to a higher membrane resistance. This suggested that back diffusion was weak with high GDL diffusivity. An article by Dai et al. (2008) reported that a hydrophobic GDL reduced water flux from the membrane to the cathode channel at all temperatures studied.

Local Water Crossover Profiles

Mench et al. (2003a) measured water mole fraction profiles along the channel direction using gas chromatography. The water mole fraction acquired increased along the channel at both anode and cathode, and was greatly dependent on inlet humidity. The current density did not significantly affect water mole fraction at the anode outlet but at the cathode outlet with dry feed, and increasing current densities yielded higher water mole

fraction. So they determined that the increase was due to generated water but not electro-osmotic drag. Dong et al. (2005) obtained similar results by using a mass spectrometer.

Nishikawa et al. (2006) put RH sensors inside various points in the flow field on the cathode side. They also obtained an increasing trend in water content along the channel, but the distribution became more and more even when cathode humidification increased. They also calculated β at the outlet, which became smaller and smaller in magnitude with increasing current densities.

Lu et al. (2007) used an approach similar to that of Mench et al. (2003a). At a voltage of 0.5 V for a fully humidified anode and partially humidified cathode, β decreased all the way from inlet to outlet. The current density decreased from the inlet and a small peak was observed near the outlet. The decrease in current density was due to the decrease in local stoichiometry, while near the outlet an increase in anode water mole fraction retained water in the membrane to give higher proton diffusivity. When the anode was unsaturated, the decreasing trend of β along the channel did not change, despite the fact that water moved from the cathode side to the anode side at the latter half of the channel. The trend in current density distribution did not change significantly when changing from a fully humidified to a partially humidified anode. Liu et al. (2007) expanded this work and found that even when dry cathode feed was used water still moved from the cathode to anode near the outlet as a result of back diffusion of product water.

Experimental Results from Dynamic Measurements

Dong et al. (2005) used a mass spectrometer with a time resolution of 1s to study a fully humidified anode and a cathode with 50% RH. At the cathode inlet, the decrease in voltage did not change the water mole fraction significantly though the current density changed from 0.9 to 0.2 Acm^{-2}. At the midpoint and close to the outlet of the cathode channel, decreasing the voltage yielded more frequent formation of water droplets.

Sur et al. (2010) used a tunable diode laser system with a time resolution of 0.2 s. They showed that their fuel cell required approximately 20 s to reach steady state under a sudden change in current. At the onset of current increase, there was a dip in water partial

pressure at the anode outlet, which was explained by the interaction among electro-osmotic drag, advection of gases before reaching the sensor and back diffusion because of water production. When the inlets were drier, more time would be required to humidify the membrane, leading to a drop in transient voltage.

Modelling studies

There are some models predicting the effect of MEA construction on water crossover. Weber and Newman (2005) used their fuel cell model to propose that the microporous layer acted as a valve to push water to the anode side through the membrane, thus reducing flooding at the cathode catalyst layer and lowered membrane resistance. However, it has been claimed by some other researchers that the GDL coatings or microporous layers help removing water at the cathode catalyst layer through the GDL but not by enhancing it. From the illustration by Pasaogullari and Wang (2004), liquid water flow is driven by the pressure gradient, which is itself dependent on the slope of the pressure-liquid saturation relationship. In a hydrophobic environment, the pores are wetted by the gas phase and there was a steeper slope in the above relationship compared to hydrophilic environments when liquid saturation levels were less than 20%. For a current density of 1.4 Acm^{-2} and with no liquid saturation at the GDL-channel interface, the liquid saturation was less than 20% for contact angles of 80˚ and 120˚. Therefore they claimed that hydrophobic coatings were advantageous in liquid water removal. However no dependence on pore size (in the form of permeability in Leverett J-function) was discussed in this article. Also the effects of water transfer to/ from the membrane were neglected.

Other related studies

Adachi et al. (2009) used different combinations of liquid and vapour feeds at the anode and cathode sides and measured the permeation of water. They explained the low rate for liquid-liquid permeation by the low chemical potential gradient involved, while the much higher liquid-vapour permeation compared to vapour-vapour permeation was explained by interfacial effects. They also compared these rates to the water transfer rates determined from running fuel cells, and found that only liquid-vapour permeation could

match the water transfer rates in running fuel cells. As a result, they suggested that liquid water was present on the cathode side of a running fuel cell.

1.6. Methods of Water Crossover Measurement

Before introducing various technologies employed in water crossover measurements, it is necessary here to point out that these methods are not directly measuring the water flow rate across the membrane. Instead, they measure the water flow rate at the outlet of the fuel cell, or at a certain point in a channel. Mass balance calculations are required to determine the total water flow rate through the membrane.

We consider first the flow of water going into a fuel cell at both anode and cathode for the purpose of humidification. Between the two electrodes there is a water transfer rate $\dot{n}_{H_2O,X}$ which is our desired quantity to measure, and also a water generation rate at the cathode catalyst layer if the oxygen reduction reaction is taking place. On the anode side, between the inlet of the anode channel to the point of water flow measurement, the change in water flow rate along the channel can only be due to water transfer. Therefore

$$\dot{n}_{H_2O,X,A} = \dot{n}_{H_2O,in,A} - \dot{n}_{H_2O,out,A} \qquad [10]$$

On the cathode side, the change in water flow rate along the channel is the result of both water transfer and water generation. This can be written as

$$\dot{n}_{H_2O,X,C} = \dot{n}_{H_2O,out,C} - \dot{n}_{H_2O,in,C} - \dot{n}_{H_2O,gen} \qquad [11]$$

Either one of the above two equations would suffice in determining the water transfer flow rate, and theoretically $\dot{n}_{H_2O,X,A}$ and $\dot{n}_{H_2O,X,C}$ should agree. In addition, the average water transfer factor α can then easily be calculated based on its definition.

Collection Methods

Water transfer rate can be obtained by the collection methods in which the water vapour or liquid water coming out from the anode and cathode channels is collected and weighed. By collecting the water in the gas streams over a certain period of time, the

water molar flow rate is found by dividing the mass of water collected by the time for collection and the molar mass of water.

The simplest method to collect water vapour in the outlet streams is to condense it by cooling. The concentration of water vapour a gas can hold depends on both temperature and pressure. Assuming that there is only gas phase in a stream, the partial pressure of water vapour in the stream is defined as (Perry and Green 2008):

$$p_{H_2O} = x_{H_2O} P = \frac{\dot{n}_{H_2O}}{\dot{n}_{total}} P \qquad [12]$$

The saturation vapour pressure of water is related to the temperature by the empirical correlations. The most common one is the Antoine equation (Poling et al. 2007):

$$\log_{10} P_{sat}(T) = 7.11564 - \frac{1687.537}{T + 230.17} \qquad [13]$$

This equation is applicable for temperatures from 0 to 200 °C. A similar alternative is the Magnus formula, applicable for temperatures from 0 to 100 °C with an error of 0.15% (Buck 1981):

$$P_{sat}(T) = 0.61121 \exp\left(\frac{17.123T}{T + 234.95}\right) \qquad [14]$$

The dew point temperature is the temperature at which the saturation pressure equals the partial pressure of water in the stream, which could be obtained by solving for T when substituting p_{H_2O} for $P_{sat}(T)$ in the above correlations.

If the temperature of the stream is lower than its dew point, the partial pressure of water vapour in a given gas stream would greater than the equilibrium vapour pressure and the excess water would condense into liquid. The flow rate of water at the outlet, in moles per second, would be

$$\dot{n}_{H_2O,out,A} = \dot{n}_{H_2O,collected,A} + \dot{n}_{drygas,out,A} \frac{P_{sat}(T_{trap})}{(P_{trap} - P_{sat}(T_{trap}))} \qquad [15]$$

Atiyeh et al. (2007) verified the saturation of the gas stream leaving the cold trap in their setup.

Condensers by chilling water are commonly used. To obtain the value of T_{trap}, some researchers controlled the temperature of the condensed water (Husar et al. 2008, Colinart et al. 2009), while measuring the temperature of air leaving the condenser has also been practised (Atiyeh et al. 2007, Dai et al. 2008). An alternative is to replace chilled water condensers by ice traps (Ge et al. 2005, 2006), so that the temperature of the air leaving the trap was kept at 0 °C due to the high latent heat of fusion of ice. However, the amount of ice has to be adequate in order to collect enough water right at 0 °C for accurate weighing.

Some authors, for the sake of simplicity, have assumed that all water vapour could be condensed by the cold trap, essentially replacing $P_{sat}(T_{trap})$ by 0. (Janssen and Overvelde 2001, Murahashi et al. 2006, Ye and Wang 2007a, Adachi et al. 2009, Colinart et al. 2009). To achieve good accuracy, the mass of the collected water is recommended to be 1000 times of the error of the balance (Ye and Wang 2007a). The typical amount of water to be collected ranged from 3 grams (Adachi et al. 2009) to 10 grams (Ye and Wang 2007a); and the typical amount of time for collection ranged from 3 to 12 hours (Ge et al. 2006). Operating the condensers at elevated pressures favours the collection of liquid water and thus minimizes the impact of the water leaving with the gas stream on the overall balance.

Although α could be calculated using the water transfer rate obtained from equation 15, cross-checking the results obtained from the anode side and cathode side measurements is common practice to ensure accuracy. Assuming a zero $P_{sat}(T_{trap})$, Janssen and Overvelde (2001) obtained a deviation of 4-7%, and 2.7-8.5% by Murahashi et al. (2006). Accounting for the amount of water left in the exhaust, Atiyeh et al. (2007) and Colinart et al. (2009) achieved deviations less than 5%. Murahashi et al. (2006) used the mean value of α from both sides in subsequent analysis. As discussed by Atiyeh et al. (2007), the accuracy of the humidification system is also important for obtaining reliable results.

The greatest advantage of using cold traps is the setup simplicity and low cost. Only condensers and balances are required. However, because of the constraints in the accuracy of balances and potential losses of liquid water after collection, a very long time is required to collect enough water to achieve an accuracy of <5% in water flow rate. Also, the measurement of mass is a batch process; cold traps are thus not suitable for transient measurements.

The water from the outlet of the cell could also be collected by sorbents prior to weighing (Yan et al. 2006). A typical sorbent for water is anhydrous calcium sulphate ($CaSO_4$), while silica gel was also employed for such purposes (Rajalakshmi et al. 2004).

The maximum amount of water that can be sorbed depends on the sorption isotherm of the sorbent chosen. For example, at 32 °C, the maximum mass of water that could be sorbed was around 5% of the mass of the $CaSO_4$ sorbent itself (Jury et al. 1972). When the sorbent can no longer take up additional moisture, a breakthrough is said to have occurred and the experimental results become erroneous. By weighing the anhydrous $CaSO_4$ before and after contact of the gases from the cell, the molar adsorption rate of water is obtained by dividing the increase in mass by the time of adsorption and the molar mass of water. Sorbents usually perform better at elevated pressures. Most spent sorbents can be regenerated by drying at low pressure and elevated temperature.

The advantage of the water sorption method over the cold traps is that a very low chilling temperature is not required. However, the ratio of mass of collected water to the error of the balance is much reduced because the water contributes only less than 5% of the measured mass (for $CaSO_4$). The accuracy on this adsorption method has not been reported for the measurement of water transport in running PEM fuel cells (Yan et al. 2006).

Dew Point Measurements

The partial pressure of water in a wet stream can be determined from dew point and relative humidity (RH) measurements. As shown above, the dew point of a stream of

wetted gas reflects the partial pressure of water in that gas stream. In addition, at a certain temperature, the relative humidity of a wetted gas is given by

$$RH = \frac{p_{H_2O}}{P_{sat}(T)} \qquad [16]$$

So the partial pressure of water can also be measured through RH. The molar flow rate of water can be determined from the partial pressure through equation 12.

It should be noted that in these methods apply to single phase gases only.

Chilled mirror sensors measure the temperature of the gas at which the first drop of water condenses (i.e. the dew point of the gas) by means of cooling a solid surface exposed to the sample gas. Unlike cold traps, the recorded quantity is the temperature rather than the mass of water, and the cooling is done gradually from the sample temperature to the dew point. Measurement is done when the first drop of condensed water is observed.

A chilled mirror sensor consists of a chamber in which a clean and highly polished mirror is placed for temperature and humidity measurement. The mirror is cooled by a Peltier cooler in which an electrical current is passed through a junction of two dissimilar conductors and the temperature of the mirror is closely monitored. The condensation of water vapour scatters a light beam originally reflected by the mirror to a detector. Then the mirror is heated by reversing the electrical current to the cooler. This is repeated until the mirror temperature and the thickness of dew is stabilized as the equilibrium is reached (Fraden 2004). So this mirror temperature would be recorded as the dew point of the gas (Bentley 1998).

Alternatively, quartz crystals can be used in place of mirrors, and optical sensing of condensation can be replaced by the change in resonance frequency. This type of sensors is termed as oscillating or piezoelectric hygrometers (Ito 1987, Fraden 2004).

The advantage of using chilled mirrors is that they are highly accurate. The uncertainty of chilled mirrors can be as low as 0.1 °C in dew point (Bentley 1998, Sauriol et al. 2009), which translates into <1.4% in terms of RH (Bentley 1998). However, thermal

equilibrium has to be achieved before readings could be taken, which translates into a penalty in response time (Sauriol et al. 2009). Piezoelectric sensors can have response times of 5 minutes from high dew point to low dew point, and 1 minute from low dew point to high dew point (Ito 1987). If there is liquid water in the stream, the dew point is above the temperature of the gas, so it is impossible to trace the dew point by means of cooling. Therefore preheating the gas prior to the sampling point of the sensor becomes necessary (Jung et al. 2007).

RH Sensors

There are two main types of RH sensors: capacitive and resistive. In capacitive RH sensors, a hygroscopic polymer changes its dielectric constant upon adsorption of moisture from the environment. When sandwiched between porous electrodes, the capacitance of the resulting capacitor increases linearly with RH (Fraden 2004). The uncertainty in the measurement is 2% RH at a RH range of 5 to 90% (Fraden 2004), while the response time is a few seconds to about four minutes for temperature and humidity.

In resistive sensors, the impedance of conductive polymers (Wilson 2005) or a layer of porous aluminum oxide (Fraden 2004) is measured. The impedance of such films could vary from 10 MΩ to 1kΩ when the RH is increased from 20 to 90%. Because of the non-linearity of the impedance response, the signal generated has to be linearized. The uncertainty of this type of sensors is 2% RH at a RH range of 15-85%, and it takes a few minutes for the sensor to respond when the RH changes from 100 to 30% (Wilson 2005).

From equation 16, a temperature reading is required to convert a RH value to the vapour pressure of water and hence water concentration. Therefore RH sensors have to be coupled with temperature sensors in order to make the reading useful (Hinds et al. 2009).

One of the advantages of using capacitive and resistive RH sensors is that they are readily available commercially at reasonable costs (Sauriol et al. 2009). Also, because of their small size and minimally disruptive nature, it is possible to place a number of these sensors in a segmented cell to investigate the changes in RH along the channel

(Nishikawa et al. 2006). However, as encountered by the dew point method, RH sensors have to operate in single-phase flows without liquid water present. Heating up the gas samples may thus be necessary. In addition, when the RH of the sample is <10%, the error increases to 10%, rendering readings unreliable. To mitigate this situation, temperature controlled RH sensors can be installed so that the RH can be maintained well above 10% (Majsztrik et al. 2008).

Composition Methods

Composition methods can directly measure the mole fraction x_{H_2O} of water vapour in a gas sample. The flow rate of water can be directly obtained using equation 12, without requiring $P_{sat}(T)$ as in the dew point and RH methods. The dew point of the sample fed to the analyzer has to be lower than the analyzer temperature to ensure all water stays vaporized.

Gas Chromatography-Thermal Conductivity Detector (GC-TCD)

In chromatography methods, the gas samples are first separated into different fractions, followed by measuring and identifying the fractions (Dean 1995). The most straightforward implementation is through gas chromatography (GC). Samples from a fuel cell are mixed with a carrier gas (usually helium) and fed into a sorbent-filled column where certain gases in the sample are more readily adsorbed on the sorbent and hence stay longer in the column. To separate small molecules like water from hydrogen, nitrogen and oxygen, columns filled with molecular sieves were commonly used (Mench et al. 2003a). To counter the problem of liquid water damage to columns and detectors, the gas fed to the column is preheated to vaporize all droplets, and the column is regularly back purged to remove water in the column (Mench et al. 2003a).

The separated components (together with the carrier gas) are fed into a detector. Because of the different column retention times, they will arrive at the detector at different times. To identify the gases, standard pure gases could be injected into the column and the retention time could serve as fingerprints of the gases. The most common detector is the thermal conductivity detector (TCD) (Dean 1995, Dimitrova et al. 2002, Mench et al.

2003a). In a TCD cell, there are two chambers: reference and sample. The reference chamber contains carrier gas only, while the samples are fed to the sample chamber. In the sample chamber, a filament is heated by current passing through it. While the thermal conductivity of the environment of the filament decreases with increasing sample content, the resistance of the filament in the sample chamber would be greater for higher sample concentrations due to a higher temperature. By measuring this resistance using a Wheatstone bridge, the concentration of a component in the sample could be found by area integration of the corresponding peak and correlating to a calibration curve (Dean 1995). The measured water molar fraction was reported to be within 4.5% error in the temperature range of 40 to 85 °C using Helium as a carrier gas (Lu et al. 2007).

The advantage of using gas chromatography is that it is possible to obtain concentrations of other species than water in the same setup and same sample. Therefore phenomena such as hydrogen crossover (Endoh et al. 2004), methanol crossover (Dimitrova et al. 2002), oxidation of water at the anode under low fuel supply (Knights et al. 2004), can be studied in addition to water transfer. Also only a very small amount of sample would suffice for the analysis by GC, and thus allows sampling of gases at specific points along the channels to measure the concentration profile of different species (Mench et al. 2003a, Yang et al. 2005, Lu et al. 2007). The typical amount of gas sampled was 20μL (Lu et al. 2007). However, since the separation of gases in the sample is based on the difference in retention times of the gases in the column, it is inevitable that significant time is required for analysis, in the order of 5 minutes (Wu et al. 2008).

The TCD alone could be used for continuous water content measurements without separation. The reference in this case would be dry gases used in the channels (Fraden 2004). Alternatively, Sauriol et al (2009) considered the possibility of using a single TCD to measure the difference in water content between the inlet and outlet gas streams. This may reduce systematic errors in the measurement. The ratio of thermal conductivity of water to that of hydrogen is 1:10 but only 1:1.4 for the water/ nitrogen or water/ oxygen pair. This makes the analysis on the cathode side more difficult (Sauriol et al. 2009). Also, at the cathode the molar ratio between nitrogen and oxygen is different between the inlet and outlet, depending on the load to the cell. Fortunately the thermal conductivity

difference between nitrogen and oxygen is only 1.2% (Chemical Rubber Company 2008), so that conductivity is barely load-dependent.

Optical Methods

In optical methods, the concentration of water in a given gas sample is measured through the absorbance of electromagnetic radiation. A source of the radiation is passed through the sample gas, and the transmitted energy intensity is detected by photon detectors. For a certain wavelength the absorbance of water is defined as

$$\Gamma = \log \frac{\Phi_{blank}}{\Phi_{sample}} \qquad [17]$$

which is dependent on the molar absorptivity, length of the optical path and the molar concentration of water vapour. The absorption band for water is around 2.4 μm. Although light in the band around 123.6 nm is also strongly absorbed by water, oxygen also shows absorption at this range, making the readings inaccurate (Auble and Meyers 1992).

Sauriol et al. (2009) used infrared gas analyzers to measure water concentrations at the cell outlet. The analyzer they used was designed for greenhouse applications (low pressure and temperature up to 50°C), and the outlet streams had to be diluted and depressurized rather than heated to vaporize any liquid water. Baseline measurements using dry gas were conducted to tackle drifts in the equipment. Also, frequent calibration against a known inlet water injection rate eliminated systematic offsets of the sensor, flow controllers and other system components in the sensor reading. By averaging values over 30 minutes, they were able to achieve an uncertainty level of 0.01 in α (Sauriol et al. 2009).

Basu et al. (2006a) passed a tunable diode laser beam of 1.491 to 1.492 μm in wavelength through a section of the flow channel to detect water. The widths of the fitted peaks in the absorption profile were used as a criterion for water vapour pressure measurement. The error level was found to be around 10% in p_{H_2O} . The measurement time for a sample was reported to be 0.4 s. The total area of the peak was found to be weakly dependent on

water vapour pressure but strongly dependent on temperature; hence temperature and water pressure could be found simultaneously (Basu et al. 2006b). An improvement was made using a wavelength modulated laser beam. The ratio between the second and first harmonics of the resultant signal was used instead of the raw absorption profile as the fitting criteria for width and area determination. The error was found to be 2.5% in p_{H_2O} and 3 °C in temperature. Also the ratio of the harmonics was independent of the incident laser intensity and system gain settings, so that the use of a background measurement could be eliminated (Sur et al. 2010).

The biggest advantage of optical methods is that it provides quick responses at a few milliseconds from the moment the sample is introduced into the measurement apparatus (Bentley 1998). In general, the measurements are highly repeatable, but the variations in the cleanliness of the optical bench, its temperature, pressure and flow rate may have an impact on the overall water transfer factor measurement. Frequent calibration (Sauriol et al. 2009), or referencing to a database (Basu et al. 2006b, Sur et al. 2010) are the solutions proposed to obtain accurate readings.

Mass Spectrometry

In mass spectrometry the gas samples are ionized and fragmented by electron beam bombardment. The ions then passed through an analyzer, most commonly a quadrupole, where an AC- DC superimposed voltage is varied to allow the passage of ions only with the desired mass-to-charge ratio. By scanning through different mass-to-charge ratios, the entire mass spectrum could be produced. It is capable of scanning up to a mass-to-charge ratio of 750 atomic mass unit per second. Ions passing through the quadrupole strike a conversion dynode which produces electron beams upon detecting ions. This is the basis of the determination of the molar ratio of a particular species in the sample (Dean 1995).

Dong et al. (2005) used a mass spectrometer (in the form of a real time gas analyzer) to detect the molar fraction of water. The samples were heated to 150 °C to have all the liquid water vaporized. The ion count from the spectrometer was calibrated using a

stream of gas at a dew point of 50 °C. The average error in molar fraction was 0.5% and the response time was around 1 s.

Similar to gas chromatography, the advantage of using mass spectrometry is the ability to study the concentration of species other than water, but with a higher degree of accuracy (Wu et al. 2010). In mass spectrometry a pure standard is even not necessary to recognize the species since molar mass information can be obtained from the spectrometer. It is minimally invasive to use mass spectroscopy in studying species distribution because of the small amount of sample required (Dong et al. 2005).

Mass Flow Methods

The total mass flow of a stream can be used to find out the corresponding water content, when the flow rates of components other than water are known. This is possible when we know the inlet gas flows, the current load of the cell, and the dry gas flow rate which could be calculated in terms of stoichiometry. Coriolis mass flow meters are good candidates. In a Coriolis mass flow meter the sample gas passes through a U shaped horizontal tube, and the mass flow rate within the tube is inversely proportional to the resonant frequency (Sparks et al. 2004).

1.7. Aims of research

From the above review it could be seen that measuring water crossover accurately is a key to study water management and hence to reduce losses in running PEMFCs. In the research project leading to this thesis, there are several goals.

1) To setup a steady state water crossover measurement apparatus and the corresponding measurement protocol. Base on the above survey on measurement technologies and considerations for other components such as water injection and gas flow controls; a repeatable, accurate and fast measurement system would be desirable for achieving fast and reliable results.

2) To study the response in water crossover of a running PEMFC with respect to different operating conditions by conducting polarization measurements. The

effects of inlet humidity, temperature and pressure as well as oxygen concentration at the cathode would be studied; and the influence of water crossover on voltage under a certain current density would also be discussed.

3) To study the effect of a microporous layer on the water crossover of a running PEMFC. Clearly from the above literature review, results on the topic have been non-conclusive, partially due to the lack of experimental data points. With efficient acquisition of data, a study with greater detail could be conducted. If possible, through the use of mechanistic models, a semi-quantitative explanation of the action of the microporous layer would be established.

4) To explore the usefulness of water crossover data in model validation and parameter estimation. Best fitted parameters would be obtained to give a qualitative examination of the powers of a selected model in explaining the experimental results in both polarization and water crossover. In addition, when sticking to that particular model, the significance of complementing polarization with water crossover data to get more accurate parameter estimates would also be studied.

2. Experimental and Model Description Methodologies

In this chapter, the approaches to obtain fuel cell performance data and to describe the behaviour of the fuel cell through the use of a quantitative mechanistic model are presented.

2.1. Experimental Setup

As discussed in the introduction, an infrared sensor is highly repeatable, sensitive and responsive, yet it does not suffer from maintenance issues with water vapour in GC systems (Mench et al., 2003a) when operating at room temperature with diluted wet gas samples. So it was chosen as the sensor for water content measurement. In addition, to ensure a stable and accurate humidification to the fuel cell, syringe pumps were used to inject liquid water into dry gas streams. This mixture was then heated to have the water vaporized, serving as the humidified feed to the fuel cell. The temperature of the preheated gas mixture was higher than the fuel cell temperature so as to ensure complete water vaporization before entering the cell. After the gas left the cell, the gas outlets were heated well above dew point before being diluted by preheated dry gas and a pressure letdown to reduce the dew point of the stream below the temperature at the infrared gas analyzer. By doing so, the noise in water concentration signals brought by condensation of water vapour between the cell outlet and the analyzer was minimized.

The flow rates of gases fed to the cell were controlled by mass flow controllers; the pressures were computer controlled through a feedback loop consisting of cell inlet pressure transducers and dome loaded pressure regulators at the outlet of the cell. The pressure drop between the inlet and the outlet of the cell was found to be less than 0.02 bar under single phase flow conditions. The dilution gases were pressure regulated using a manual pressure regulator while the flow rates were monitored using mass flow meters. The dilution gas flows were found to fluctuate with a standard deviation below 2.98×10^{-5} $mols^{-1}$, which was less than 0.2% of the total flow during operation. The temperature of the cell was regulated by a water coolant stream that ran through the flow field plates. This stream was in turn controlled by a PID heater controller, which could stabilize the

cell temperature within one hour after startup. The high flow rate of the coolant acted as a heat reservoir to ensure high uniformity in temperature at different parts of the cell, while also brought the inlet gas temperature quickly to the operating temperature. A constant current was drawn by a load bank while both the actual current and voltage of the cell were recorded. The schematic diagram of the system is presented in Figure 3 (a).

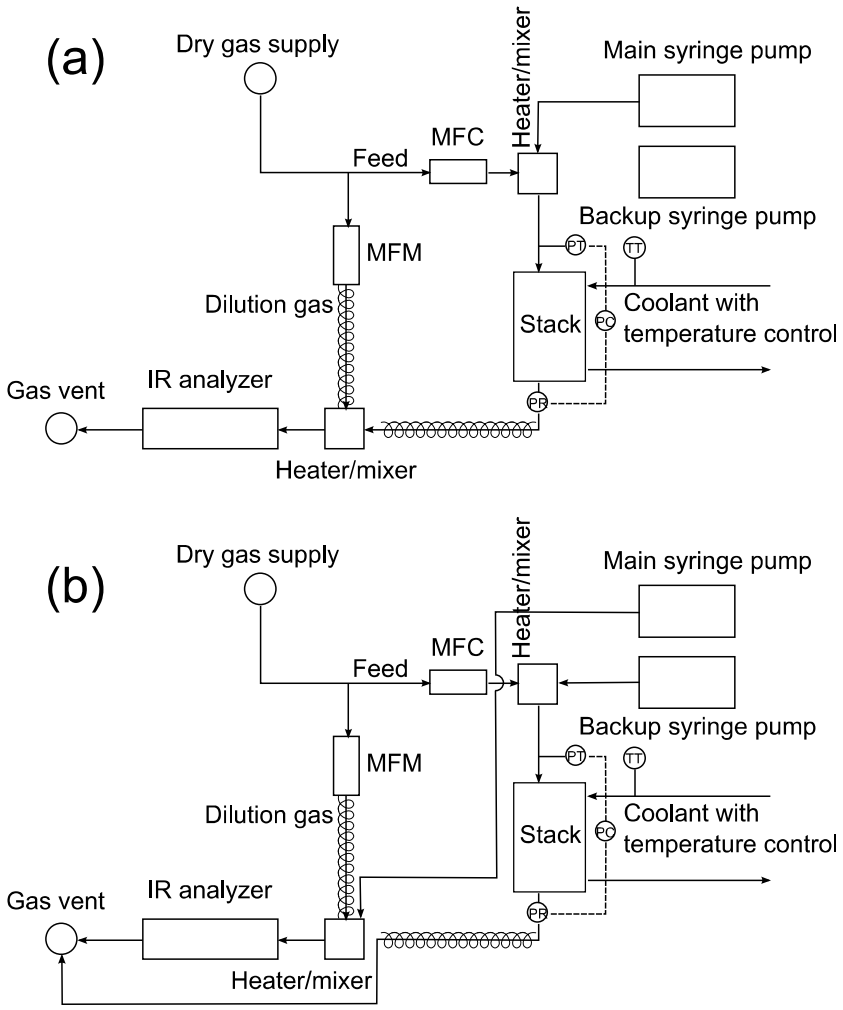

Figure 3. Schematic diagram of the experimental setup. Only one side/ electrode of the setup is shown for simplicity. (a) The configuration for 'normal mode' measurements, when the water crossover rate for the fuel cell is measured. (b) In the 'calibration mode', liquid water from the main syringe pump, which is the feed to the fuel cell during normal operations, is fed directly to mix with the dilution gas from MFM and then analyzed by the IR as a reference reading. The operation of the fuel cell is kept continuous by using a backup system to supply humidified gases. The outlet gases from the cell are purged to the vent.

2.2. MEA Construction and Operating Conditions

In all the experiments single cells were tested. The MEAs were put between flow field plates with parallel channels for the gases on one side, and channels for coolant flow on the other side. Since both MEA construction and operating conditions were varied according to the purpose of the tests, they will be introduced in the next two chapters which are dedicated to those tests.

2.3. Equipment Calibration Procedures

To eliminate systematic errors from different components, calibration steps were implemented. The water concentrations of a gas stream with known water content and known flow rate, created by the same syringe pump and flow meter as would be used during the 'normal' operation, were monitored by the same infrared sensor in calibration (see Figure 3(b)). During calibration tests, the feed streams were humidified by the backup syringe pump so as to bring minimal disturbance to the operation of the cell. As water crossover rate was calculated from the difference between inlet and outlet water flows, this approach yielded a more accurate determination of the crossover flux, in comparison to the traditional approaches since the subtracted terms involved in the calculation came from the same equipment (in this case, the molar flow rate from the syringe pump). Therefore the systematic errors of the equipment were cancelled out.

For the *j*-th calibration point, the expected concentration of the sensor averaged for over a period of time no less than 15 minutes was given by

$$y'_{j,cal} = \frac{\dot{n}_{j,H_2O,cal}}{\bar{\dot{n}}_{j,drygas,cal}} \qquad [18]$$

whereas the average measured concentration was $\bar{y}_{j,H_2O,cal}$. A calibration line was established through the measurement of at least three known water concentrations, $j \geq 3$. Also these measurements were made right before and after each 'normal' test, to minimize the effect of temperature drifts in the lab throughout the experiments.

A calibration curve with which measured readings were converted to expected concentrations, was obtained by linear least squares fitting (Beers 2007). The line was in the form of $y' = m'\bar{y}_{H_2O} + c'$, where the slope was

$$m' = \frac{1}{N}\sum_j y'_{j,cal} - \frac{\sum_j \bar{y}_{j,H_2O,cal} y'_{j,cal} - \frac{1}{N}\sum_j \bar{y}_{j,H_2O,cal}\sum_j y'_{j,cal}}{\sum_j \left(\bar{y}_{j,H_2O,cal}\right)^2 - \frac{1}{N}\left(\sum_j \left(\bar{y}_{j,H_2O,cal}\right)\right)^2}\left(\bar{y}_{j,H_2O,cal}\right) \qquad [19]$$

and the intercept was

$$c' = \frac{\sum_j \bar{y}_{j,H_2O,cal} y'_{j,cal} - \frac{1}{N}\sum_j \bar{y}_{j,H_2O,cal}\sum_j y'_{j,cal}}{\sum_j \left(\bar{y}_{j,H_2O,cal}\right)^2 - \frac{1}{N}\left(\sum_j \left(\bar{y}_{j,H_2O,cal}\right)\right)^2} \qquad [20]$$

A minimum of 50 minutes of actual fuel cell outlet concentration data were used to obtain a steady reading and averaged. Using this calibration line, the water crossover rate at the anode was calculated by

$$\dot{n}_{H_2O,X,A} = \dot{n}_{H_2O,in,A} - \frac{m'_A \bar{y}_{H_2O,out,A} + c'_A}{1 - \left(m'_A \bar{y}_{H_2O,out,A} + c'_A\right)}\left(\dot{n}_{MFC,A} + \dot{n}_{MFM,A} - \frac{\bar{I}A}{2F}\right) \qquad [21]$$

and

$$\dot{n}_{H_2O,X,C} = \frac{m'_C \bar{y}_{H_2O,out,C} + c'_C}{1 - \left(m'_C \bar{y}_{H_2O,out,C} + c'_C\right)}\left(\bar{\dot{n}}_{MFC,C} + \bar{\dot{n}}_{MFM,C} - \frac{\bar{I}A}{4F}\right) - \dot{n}_{H_2O,in,C} - \frac{\bar{I}A}{2F} \qquad [22]$$

The average water crossover flux $\bar{J}_{H_2O}$ is defined by the water crossover rate per unit active cell area:

$$\bar{J}_{H_2O} = \frac{\dot{n}_{H_2O,X,A}}{A} = \frac{\dot{n}_{H_2O,X,C}}{A} = \frac{\dot{n}_{H_2O,X}}{A} \qquad [23]$$

It was shown (Sauriol et al., 2009) that the measurement error in the water crossover coefficient α of less than ±0.01 could be achieved in validation experiments using one point calibration. In addition, as found from experiments described in Chapter 4, repeatability in water crossover flux measurements was good using the new linear calibration approach. The maximum difference in flux measurement across 2 different MEAs with identical construction and under the same condition was less than 1.74×10^{-7} $molcm^{-2}s^{-1}$, which was equivalent to water generation at a current density of 34 $mAcm^{-2}$ at the anode channel. That corresponded to 1.7% of the water injected, and was significantly better than 4.5% reported from GC measurements (Lu et al. 2007).

Beyond this point in the thesis, the quantities 'current density' and 'water crossover flux' refer to their overall values averaged over the whole active cell area, unless otherwise specified.

2.4. Model Description

In this thesis, a model proposed by Berg et al. (2004) would be used as a basis to examine hypotheses describing the effect of the microporous layer on water crossover, as well as to demonstrate the value of water crossover data in model validation and parameter estimation. A concise description of the model would be presented in this section, and in the following chapters this model would be referred to as the 'Berg model'.

The key features in this steady state 1+1 dimensional model are:

1) transport within the membrane occurs only in the through-the-membrane direction;

2) concentration of water in the membrane is different at every location along the channel by coupling interfacial conditions with channel flow and through the membrane direction;

3) flow rates within the channel change along the channel direction only;

4) at the membrane/gas interface, water transfer is proportional to the difference between equilibrium water content and the water content at the membrane surface;

5) the gas diffusion layer (GDL) acts as a diffusive barrier for oxygen, while liquid and vapour water could leave the gas diffusion layer freely;

6) any liquid water formed is considered as droplets with zero volume;

7) the gases are assumed to be ideal;

8) pressure within the cell is assumed to be constant;

9) landings are disregarded;

10) EOD coefficient equals 1 (one molecule of water dragged per proton) for all membrane water contents.

There are four parameters which have to be fitted to the data obtained from experiments, namely the membrane interfacial water transfer coefficient γ, oxygen diffusivity factor δ (which is related to the effective diffusivity of oxygen in the GDL D_{G,O_2} by $\delta = \frac{L_G}{4FD_{G,O_2}}$), exchange current density $i_{o,c}$, and the effective membrane conductivity σ, which is defined as the inverse of the membrane resistance at full humidification.

In this thesis it was further assumed that:

1) the cell is isothermal and isobaric-along-the-channel;

2) the voltage was constant along the channel direction and in different channels;

3) the potential determined at the bus plates is considered to be the same as that at the catalyst layer;

4) the reactants are uniformly distributed between different channels.

For each point on the polarization curve, cell voltage, cell geometry, material properties and other experimental conditions including temperature, pressure, gas flow rates and water flow rates were fed into the program to obtain a current density at a differential length, by solving equation 49 of Berg et al. (2004) Then all relevant properties, including current density, water crossover and flow rates of different species at both electrodes, were integrated. The overall current density was given by

$$\bar{I}_{model} = \frac{\int_0^{L_C} I dx}{L_C} \qquad [24]$$

and the overall water crossover flux was given by

$$\bar{J}_{H_2O,model} = \frac{N_C L_w}{A \times 10^{-4}} \int_0^{L_C} J_{H_2O} dx \qquad [25]$$

As these two quantities are measurable by the equipment described above, they would serve as the basis for comparison between model predictions and experimental results. The predicted values from the model, given a set operating conditions and fuel cell properties, still depend highly on the values of the four model parameters. They would be obtained by fitting model predictions to experimental data. The procedures for model fitting would be described in detail in Chapter 5 before the model was used for further analysis of changes in conditions.

3. Effects of Operating Conditions on Water Crossover

In this chapter, the polarization and water transport behaviour of a fuel cell in response to various operating conditions was explored. These parameters included temperature, pressure, inlet RH and oxygen content. Their effects on voltage and water crossover at different current densities would be discussed, from a mass transport point of view. The analysis would be based on the assumption that the cell was isothermal and heat effects would be neglected. As mentioned in the experimental section, the low pressure drop in the cell due to gas flow led to an isobaric-along-the-channel assumption in the analysis.

3.1. Cell Construction and Experimental Conditions

The thickness of the polymer electrolyte membrane was 25 microns and the MEA area was 50 cm^2. Undiluted hydrogen was used on the anode side while on the cathode side nitrogen-oxygen mixtures of various compositions were used. Both anode and cathode streams were humidified, and ran co-currently. The flow rates were kept constant during the acquisition of the polarization curves.

Table 1 summarizes the conditions used in the 9 runs conducted. The polarization curves generally consisted of 9 measurement points. For each point on the curve, a constant current was withdrawn from the load bank and the cell voltage was measured, along with the water crossover flux determined from the measurement taken from the anode and cathode streams in accordance to the equations 21 and 22 respectively.

3.2. Results and Discussion

Figure 4 shows the polarization curves for runs 1 to 6. As expected, a higher current density could be withdrawn at a higher oxygen concentration. Compared to run 1, run 6 gave a better *I-V* performance in the ohmic region, indicating that the use of a wetter anode provides better water management and membrane humidification. On the anode side the higher RH made membrane dry-out less likely.

Table 1. Inlet conditions employed in polarization curve experiments.

Run	Temperature (˚C)	Anode pressure (kPa)	Cathode pressure (kPa)	H_2 flow rate ($mols^{-1}$)	N_2 flow rate ($mols^{-1}$)	O_2 flow rate ($mols^{-1}$)	O_2 mol % (dry basis)	Anode RH (%)	Cathode RH (%)
1	60	230	200	3.13×10^{-3}	2.98×10^{-3}	7.46×10^{-4}	20	25	75
2	60	230	200	3.13×10^{-3}	3.17×10^{-3}	5.59×10^{-4}	15	25	75
3	60	230	200	3.13×10^{-3}	3.36×10^{-3}	3.73×10^{-4}	10	25	75
4	60	230	200	3.13×10^{-3}	3.56×10^{-3}	1.86×10^{-4}	5	25	75
5	60	230	200	3.13×10^{-3}	3.64×10^{-3}	9.32×10^{-5}	2.5	25	75
6	60	230	200	3.13×10^{-3}	2.98×10^{-3}	7.46×10^{-4}	20	75	25
7	70	230	150	3.13×10^{-3}	2.98×10^{-3}	7.46×10^{-4}	20	25	75
8	70	230	200	3.13×10^{-3}	2.98×10^{-3}	7.46×10^{-4}	20	25	75
9	70	230	250	3.13×10^{-3}	2.98×10^{-3}	7.46×10^{-4}	20	25	75

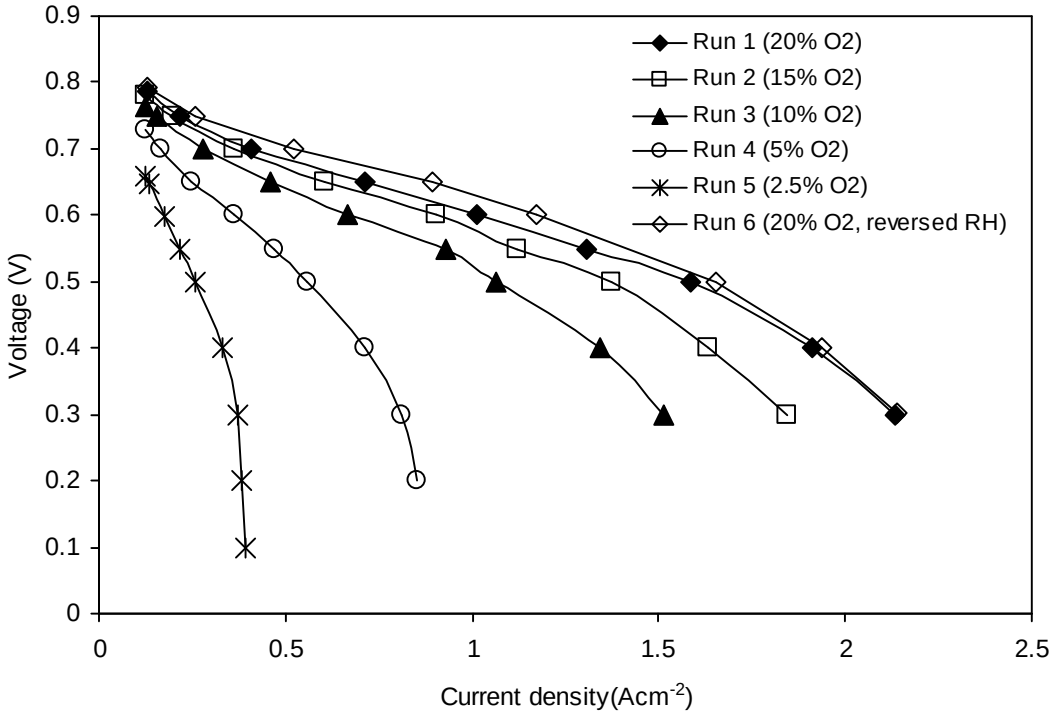

Figure 4. Experimental polarization curves at constant fuel and oxidant flow rates for runs 1 to 6. O_2 concentrations on the cathode are as indicated. T = 60 °C, P_A = 230 kPa, P_C = 200 kPa. For runs 1 to 5, $RH_{in,A}$ = 25%, $RH_{in,C}$ = 75%. For run 6, $RH_{in,A}$ = 75%, $RH_{in,C}$ = 25%. H_2 flow rate = 3.13×10^{-3} $mols^{-1}$, N_2 and O_2 total flow rate = 3.73×10^{-3} $mols^{-1}$.

The water crossover flux measured at the cathode side was always greater than that measured at the anode side. The difference between the two readings is presented in Figure 5. The difference has an average value of 1.88×10^{-7} molcm^{-2}s^{-1}, or an equivalent current density of 3.45×10^{-3} Acm^{-2}. This was probably not due to errors because the paired t-test showed the probability of no difference between anode and cathode readings was at an order of 10^{-33}. A possible explanation is that this additional water flux from anode to cathode, while not contributing to any external current, was due to hydrogen crossover which gets converted to water at the cathode catalyst layer. This crossover flux increased with current density, similar to the findings from measured hydrogen crossover in a fuel cell under different RH by Cheng et al. (2007) at 80 ˚C, 3.04 atm backpressure without load. They explained such results by the increased membrane water content at high RH and the consequent increase in hydrogen solubility and diffusivity. The same reasoning could be applied to the situation here as the membrane water content increased with increasing water transfer from cathode to anode. Kocha et al. (2006) obtained a hydrogen permeability ψ of 3.32×10^{-14} molm^{-1}s^{-1}Pa^{-1} at 60 ˚C, from experiments on Nafion 111 and 112. The equivalent current density could be calculated by

$$I_{H_2} = \frac{2F\psi\left(P_{H_2,A} - P_{H_2,C}\right)}{L_m \times 10^4} \qquad [26]$$

to yield a value of 5.89×10^{-3} Acm^{-2}. These results indicate a significant increase of hydrogen crossover under current load, although the reason behind this discrepancy requires further studies. In order to avoid ambiguity, the water crossover data obtained from the anode side are used beyond this point.

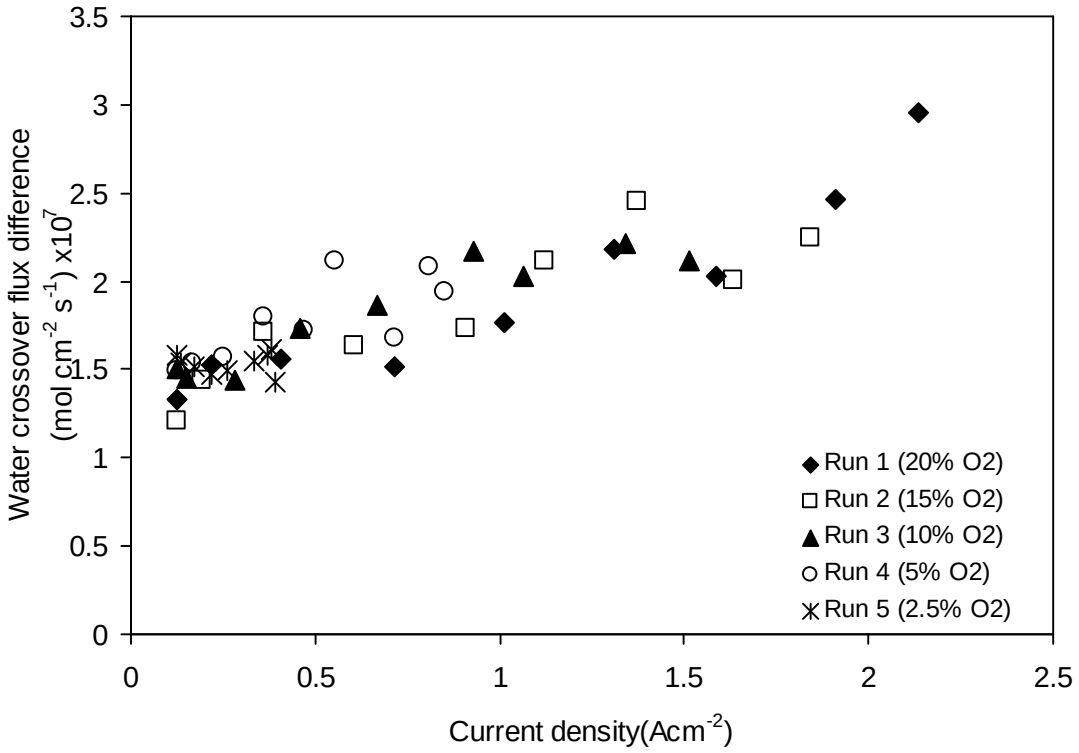

Figure 5. Difference between water crossover fluxes measured from anode and from cathode in runs 1 to 5. O_2 concentrations on the cathode are as indicated. T = 60 °C, P_A = 230 kPa, P_C = 200 kPa, $RH_{in,A}$ = 25%, $RH_{in,C}$= 75%. H_2 flow rate = 3.13×10^{-3} $mols^{-1}$, N_2 and O_2 total flow rate = 3.73×10^{-3} $mols^{-1}$. The positive values indicate that a greater anode-to-cathode water transfer is observed from the cathode, which can be interpreted as the result of hydrogen crossover from anode to cathode.

The relationship between water crossover flux and current density is shown in Figure 6. For runs 1 to 5, all values of water crossover flux were negative, while for run 6, the values were negative for current densities greater than 0.8 Acm^{-2}. When the current density increased, the water generated by the electrochemical reaction at the cathode side of the membrane became an additional driving force for water going from the cathode to the anode which dominated over electro-osmotic drag. Interestingly, water crossover flux was a highly linear function of current density regardless of oxygen concentration, with a correlation coefficient (R^2) of 0.989, up to around 1.5 Acm^{-2}, and above that a slightly less negative slope was observed. The linear result was coherent with those obtained with

oversaturated channels by Husar et al. (2008). Atiyeh et al. (2007) found that the anode-to-cathode water transfer rate decreased with increasing current density at saturated cathode and 60% RH anode at 60 ˚C using microporous layered cathode. Contrarily, Janssen and Overvelde (2001) showed that water crossover flux with saturated gases increased with current density. When dry anode and saturated cathode feeds were used, water crossover flux decreased linearly with current density, consistent with our results, although theirs was dependent on hydrogen stoichiometry. Colinart et al. (2009) also obtained greater cathode to anode water transfer rate by increasing the current density, using dry anode and 70% RH cathode.

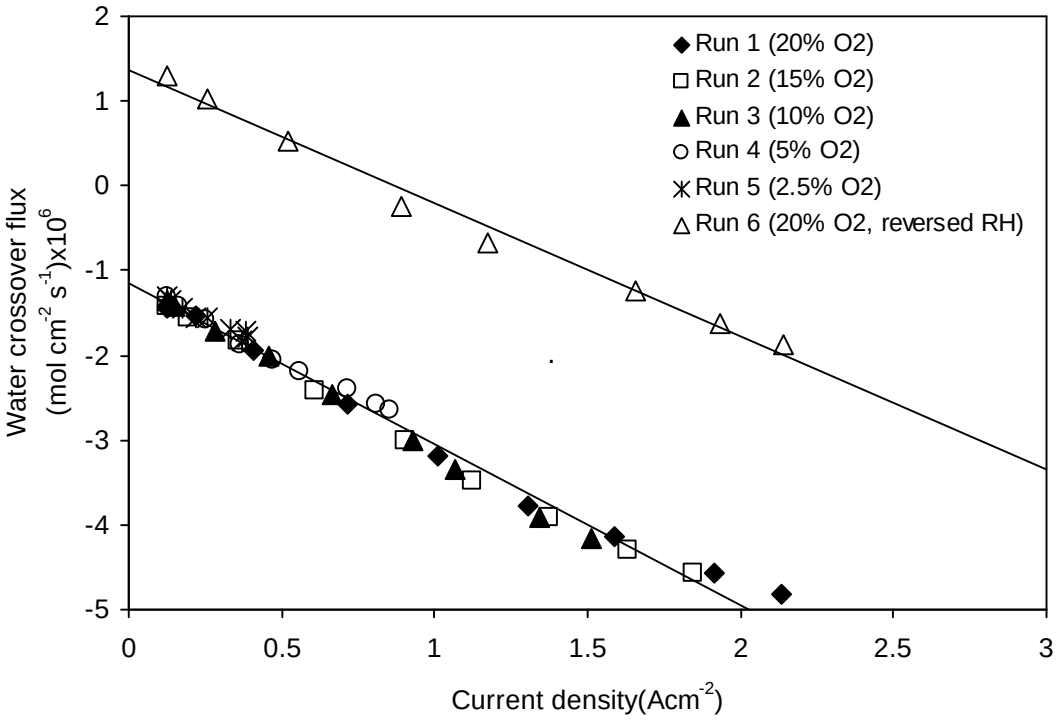

Figure 6. Water crossover flux (measured from anode) against current density for runs 1 to 5 (lower line) and run 6 (upper line). Negative values indicate water transfer from cathode back to anode. T = 60 °C, P_A = 230 kPa, P_C = 200 kPa. For runs 1 to 5, $RH_{in,A}$ = 25%, $RH_{in,C}$= 75%. For run 6, $RH_{in,A}$ = 75%, $RH_{in,C}$ = 25%. H_2 flow rate = 3.13×10^{-3} $mols^{-1}$, N_2 and O_2 total flow rate = 3.73×10^{-3} $mols^{-1}$.

The non-zero intercept for runs 1 to 5 in Figure 6 was an expected result, since in these runs the anode RH was less than the cathode RH, so water vapour at the cathode diffused to the anode by concentration gradient at zero current density. The intercepts for runs 1-5 were not significantly different, as expected, since the water vapour concentrations on both anode and cathode were the same in these runs, showing that the different concentrations of oxygen had little effect on the diffusion of water vapour within the GDL. The 90% confidence interval for this intercept was found to be $(-1.14\pm0.055)\times10^{-6}$ $molcm^{-2}s^{-1}$. For run 6, with the anode and cathode RH's reversed, a value of $(1.36\pm0.22)\times10^{-6}$ $molcm^{-2}s^{-1}$ was found. Therefore, under these experimental conditions, the absolute values of intercepts were not significantly different, indicating anode/cathode symmetry of the fuel cell design with respect to water crossover. Using the intercept of $(-1.14\pm0.055)\times10^{-6}$ $molcm^{-2}s^{-1}$ the value of membrane interfacial water transfer coefficient γ could be estimated using equations 42−44 in Berg et al. (2004) γ was found to be $(9.89\pm0.91)\times10^{-6}$ ms^{-1}, which is in the same order of magnitude as those values reported by Berg et al. (2004).

As shown in Figure 7, the water transported from the cathode catalyst layer through the cathode GDL is the sum of the anode-to-cathode water flux and water generation by the oxygen reduction reaction:

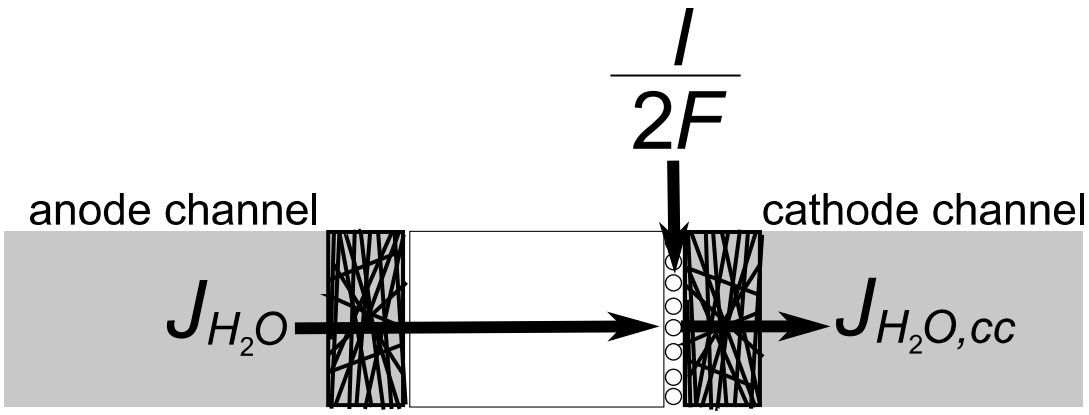

Figure 7. Mass balance of water around the cathode catalyst layer.

$$J_{H_2O} + \frac{I}{2F} = J_{H_2O,cc} \qquad [27]$$

The average fluxes $\bar{J}_{H_2O}$, $\bar{J}_{H_2O,cc}$ and the average current density $\bar{I}$ were obtained by integration along the channel direction. Differentiating against $\bar{I}$, dividing by the total active area and rearranging terms one arrives at

$$\frac{1}{2F} = -\frac{\partial \bar{J}_{H_2O}}{\partial \bar{I}} + \frac{\partial \bar{J}_{H_2O,cc}}{\partial \bar{I}} \qquad [28]$$

The incremental water generation flux under increasing current is $\frac{1}{2F}$ (5.18×10^{-6} $molA^{-1}s^{-1}$). This incremental water produced is split either to the anode, denoted by $-\frac{\partial \bar{J}_{H_2O}}{\partial \bar{I}}$ or to the cathode, denoted by $\frac{\partial \bar{J}_{H_2O,cc}}{\partial \bar{I}}$. From the experimental results, the slope of the line $-\frac{\partial \bar{J}_{H_2O}}{\partial \bar{I}}$ is constant for a given set of T, P and inlet RH, and thus it is easy to determine an average product water split between cathode and anode. The results from runs 1 to 5 at current densities less than 1.5 Acm^{-2} give $-\frac{\partial \bar{J}_{H_2O}}{\partial \bar{I}}$ = $(1.91\pm0.062)\times10^{-6}$ $molA^{-1}s^{-1}$ and a corresponding $\frac{\partial \bar{J}_{H_2O,cc}}{\partial \bar{I}}$ =$(3.27\pm0.062)\times10^{-6}$ $molA^{-1}s^{-1}$. Hence on average 63.1% of the water generated ended up in the cathode stream. Similarly, it was determined that under conditions for run 6 which differs in inlet RH, $-\frac{\partial \bar{J}_{H_2O}}{\partial \bar{I}}$ = $(1.57\pm0.17)\times10^{-6}$ $molA^{-1}s^{-1}$ and so 69.7% of the water generated ended up in the cathode stream. The inlet RH gradient appears to play a minor role in how this water was distributed.

At higher current densities, as described earlier the slope was found to be less negative. An increase in slope of the curve indicated a drop in back diffusion in comparison to electro-osmotic drag, if a constant electro-osmotic drag coefficient with respect to water content was assumed (Zawodzinski et al. 1995). The drop in back diffusion was probably

caused by a decrease in concentration gradient across the membrane. When the cathode interface of the membrane was saturated or very close to saturation, back diffusion only increased the water content at the anode interface and in turn yielded a smaller concentration gradient. Despite decreased back diffusion, the water crossover flux was still negative because the magnitude of back diffusion was still greater than that of electro-osmotic drag.

By measuring water transfer through Nafion 112 membranes ex-situ, Adachi et al. (2009) showed that the strong 'backward transport' of water from cathode to anode in their running fuel cells could be sustained only if water was in liquid state at the cathode side, and vapour state at the anode side. Murahashi et al. (2006) also suggested the presence of liquid water in micro pores due to a high vapour pressure, which enabled a stable operation of Buchi et al.'s experiments at 60 ˚C under dry air conditions (Buchi and Srinivasan 1997). However, assuming the presence of liquid water at the catalyst layer at all current densities, our experimental results contradicted the arguments by authors like Ge et al. (2005) and Monroe et al. (2008) that when in contact with liquid water, the membrane-liquid water interface was immediately at equilibrium yielding saturation. If that were true, the water concentration gradient across the membrane could not be greater than that at the lowest current density when the cathode side of the membrane was saturated. Therefore, an increasing back-diffusion with increasing current density would not be possible in that case and the water crossover flux would deviate from the observed behaviour with current density.

The effect of cathode pressure on polarization was shown in Figure 8. Higher pressure meant higher oxygen concentration and so yielded better performance in both ohmic and mass transport regions. Interesting results were observed from the water crossover flux-current density relationship in Figure 9. The intercepts for the three runs were close to -1.06×10^{-6} $molcm^{-2}s^{-1}$ for the conditions studied. This more negative intercept compared to runs 1 to 5 was probably due to the operation at a higher temperature of 70 °C which enhanced mass transport processes from the cathode back to the anode. On the other hand, the trends in the slopes clearly showed that with cathode pressure increasing from 150 kPa to 250 kPa, the slopes changed from $(-6.6\ \pm1.4)\times10^{-7}$ $molA^{-1}s^{-1}$ to

$(-2.06\pm0.083)\times10^{-6}$ $molA^{-1}s^{-1}$. Yan et al. (2006) also observed decreasing water crossover coefficients when the cathode pressure was increased.

The influence of the cathode side pressure on the split between cathode and anode was important. From runs 7 to 9, 87.3%, 77.9% and 60.2% of the generated water ended up in the cathode for cathode pressures of 150, 200 and 250 kPa respectively. Pure hydraulic permeation does not provide a satisfactory explanation to the experimental results because in runs 7 and 8, where the pressure at the anode was higher than that at the cathode, it was not possible to cause water transport back to the anode. The relative humidity at any point in the anode and cathode channels were governed by

$$RH_C = \frac{\dot{n}_{H_2O,in,C} + 10^4 \int_0^{L_c'} \left(\frac{I}{2F} + J_{H_2O} \right) L_w dx}{\dot{n}_{total,in,C} + 10^4 \int_0^{L_c'} \left(\frac{-I}{4F} + \frac{I}{2F} + J_{H_2O} \right) L_w dx} \frac{P_C}{P_{sat,H_2O}} \quad [29]$$

$$RH_A = \frac{\dot{n}_{H_2O,in,A} - 10^4 \int_0^{L_c'} J_{H_2O} L_w dx}{\dot{n}_{total,in,A} - 10^4 \int_0^{L_c'} \left(\frac{I}{F} + J_{H_2O} \right) L_w dx} \frac{P_A}{P_{sat,H_2O}} \quad [30]$$

$$RH_A - RH_C = \frac{\dot{n}_{H_2O,in,A} - 10^4 \int_0^{L_c'} J_{H_2O} L_w dx}{\dot{n}_{total,in,A} - 10^4 \int_0^{L_c'} \left(\frac{I}{F} + J_{H_2O} \right) L_w dx} \frac{P_A}{P_{sat,H_2O}} - \frac{\dot{n}_{H_2O,in,C} + 10^4 \int_0^{L_c'} \left(\frac{I}{2F} + J_{H_2O} \right) L_w dx}{\dot{n}_{total,in,C} + 10^4 \int_0^{L_c'} \left(\frac{-I}{4F} + \frac{I}{2F} + J_{H_2O} \right) L_w dx} \frac{P_C}{P_{sat,H_2O}} \quad [31]$$

Along the cathode channel, the change in total gas flow was small compared to the change in water flow. Therefore, for the same current density, a higher overall pressure yielded a greater gradient in relative humidity across the membrane downstream and hence more back diffusion.

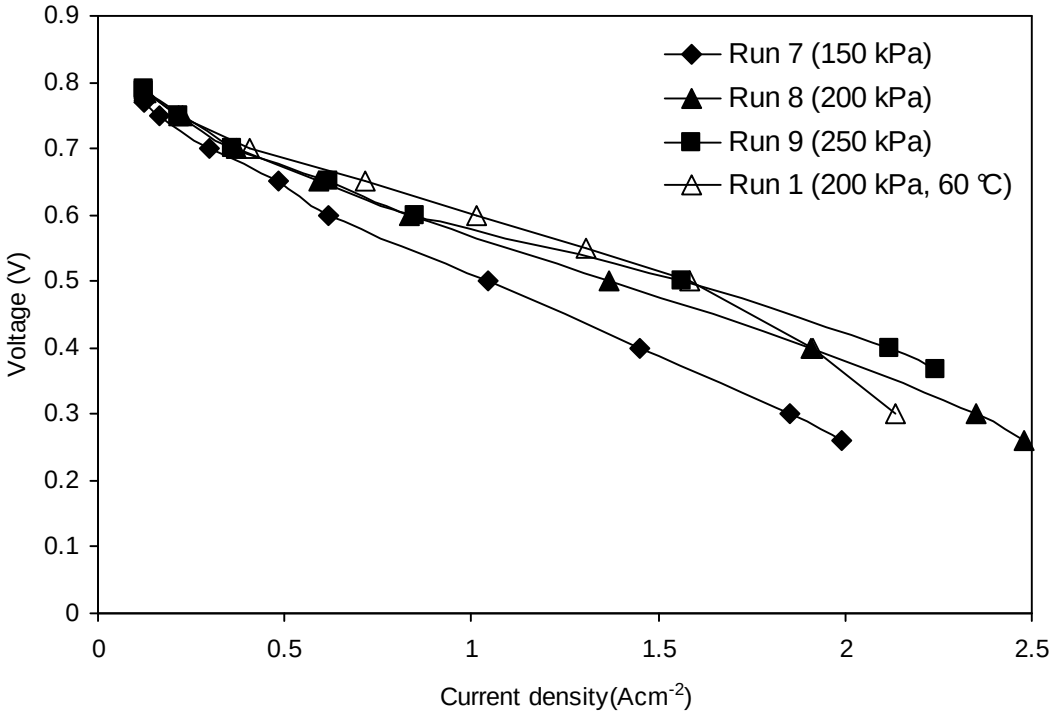

Figure 8. Experimental polarization curves at constant fuel and oxidant flow rates for run 1 and runs 7 to 9. Cathode pressures are as indicated. For run 1, T = 60 °C. For runs 7 to 9, T = 70 °C P_A = 230 kPa, $RH_{in,A}$ = 25%, $RH_{in,C}$ = 75%. H_2 flow rate = 3.13×10^{-3} $mols^{-1}$, N_2 flow rate = 2.98×10^{-3} $mols^{-1}$, O_2 flow rate = 7.46×10^{-4} $mols^{-1}$.

The effects of temperature on polarization and water crossover can be observed in Figure 8 and Figure 9 from runs 1 and 8. In the mass transport limiting region run 1 gave a higher voltage than run 8. This was an expected result due to an increased effective diffusivity of oxygen at an elevated temperature in run 8. In the ohmic region run 1 gave a higher voltage. The lower temperature in run 1 resulted in more product water migrating to the anode stream through the membrane (36.9% compared to 27.2% in run 8), and hence a lower membrane resistance. The increase in water saturation vapour pressure P_{sat,H_2O} at a higher temperature seemed to dominate over the effects of the increased mass transport coefficients. So the RH gradient would be lower along the cell at 70 °C and caused less back diffusion.

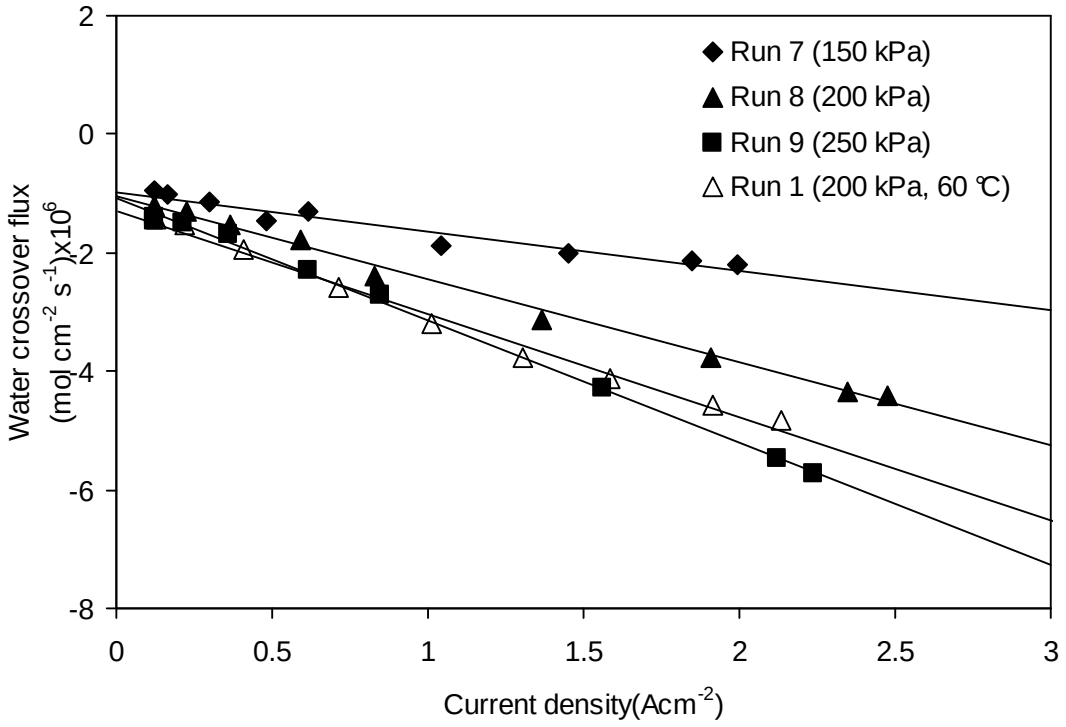

Figure 9. Water crossover flux (measured from anode) against current density for run 1 and runs 7 to 9. Negative values indicate water transfer from cathode back to anode. Cathode pressures are as indicated. For run 1, T = 60 °C. For runs 7 to 9, T = 70 °C P_A = 230 kPa, $RH_{in,A}$ = 25%, $RH_{in,C}$ = 75%. H_2 flow rate = 3.13×10^{-3} $mols^{-1}$, N_2 flow rate = 2.98×10^{-3} $mols^{-1}$, O_2 flow rate = 7.46×10^{-4} $mols^{-1}$.

3.3. Roundup

The water crossover flux measured on the cathode side was consistently higher than that measured on the anode side. The difference was interpreted as a result of hydrogen crossover across the membrane, which generated additional water at the cathode. Anode-to-cathode water crossover fluxes of a concurrent flow fuel cell at 60 ˚C and undersaturated feeds were found to be highly linear with respect to current density up to 1.5 Acm^{-2}, regardless of the oxygen concentration in the gas feed. This suggests a constant distribution of water produced by the oxygen reduction reaction through the membrane and through the GDL. The inlet humidity gradient between anode and cathode

affected the intercept of the water crossover flux- current density line, while the slope was only insignificantly affected. From the intercepts, the membrane interfacial transfer coefficient γ was found to be $(9.89\pm0.91)\times10^{-6}$ ms^{-1}. Increasing cathode pressures yielded steeper negative slope and hence the water distribution leaned more to the anode side. Increasing temperatures changed the water distribution to the other direction. This was because the generated water led to a higher RH gradient along the channel with increasing cathode pressures but a lower gradient downstream with increasing temperatures.

4. Effects of Microporous Layer on Water Crossover

In the literature review, it has been discussed that the effect of the microporous layer (MPL) on water crossover is still in debate. Since the setup described in this thesis is of high accuracy and able to collect water crossover data quickly, it can provide accurate and adequate data in light of resolving the discrepancy. As in the previous chapter, the analysis would be based on isothermal and isobaric-along-the-channel assumptions.

4.1. MEA Construction and Experimental Conditions

4 pieces of catalyst coated Nafion NRE211 membranes with an area of 50 cm^2 were assembled with different gas diffusion layers made from PTFE coated Toray carbon paper. Two of the MEAs had MPLs on both anode and cathode, and the other two had MPLs on the anode side only. Each pair of identically constructed MEAs served as replicates to check for reproducibility of the results. From this point on, the set of MEAs with microporous layer on the cathode would be denoted by “with MPL” and the other set would be denoted by “without MPL”.

Table 2 summarizes the conditions used in the polarization experiments. The effects of MPL as well as inlet RH gradient between anode and cathode were studied. To minimize the effect of pressure on water crossover, both anode and cathode pressures were kept at 230kPa (absolute). Each MEA was subjected to two different humidity conditions. A polarization curve was created by running the cell at 7 different current densities; and to avoid the possible effects of hysteresis, the order for different current densities in the polarization curve was randomized for each run. The dry gas flow rates were constant under different current densities.

Table 2. Inlet conditions employed in polarization curve experiments.

Run	MEA #	With MPL?	Temperature (°C)	Anode pressure (kPa)	Cathode pressure (kPa)	H_2 flow rate ($mols^{-1}$)	N_2 flow rate ($mols^{-1}$)	O_2 flow rate ($mols^{-1}$)	Anode RH (%)	Cathode RH (%)
10	1	No	70	230	230	4.46×10^{-3}	2.94×10^{-3}	7.81×10^{-4}	75	25
11	1	No	70	230	230	4.46×10^{-3}	2.94×10^{-3}	7.81×10^{-4}	75	75
12	2	No	70	230	230	4.46×10^{-3}	2.94×10^{-3}	7.81×10^{-4}	75	25
13	2	No	70	230	230	4.46×10^{-3}	2.94×10^{-3}	7.81×10^{-4}	75	75
14	3	Yes	70	230	230	4.46×10^{-3}	2.94×10^{-3}	7.81×10^{-4}	75	25
15	3	Yes	70	230	230	4.46×10^{-3}	2.94×10^{-3}	7.81×10^{-4}	75	75
16	4	Yes	70	230	230	4.46×10^{-3}	2.94×10^{-3}	7.81×10^{-4}	75	25
17	4	Yes	70	230	230	4.46×10^{-3}	2.94×10^{-3}	7.81×10^{-4}	75	75

4.2. Results and Discussion

Figure 10 shows the polarization curves for different conditions. The results presented are the average from two different MEAs with the same construction. Reproducibility was satisfactory with the difference in voltage being less than 31 mV between replicates.

The difference between the four combinations of MEA construction and RH was negligible for current densities <0.3 Acm^{-2}. Feed humidification and the addition of MPL had little effect on the kinetics of the electrochemical reaction. In the ohmic region, the addition of MPLs did give rise to a higher cell voltage at the same current density, but the effect was not as significant as using higher cathode gas humidification. It could be deduced that the membrane water content could be enhanced by a high RH at both anode and cathode, leading to a lower ohmic resistance. When the RHs of both anode and cathode feed streams were 75%, the difference in voltage brought by the addition of MPL became larger at current densities >1.5 $mAcm^{-2}$. The transport resistance may be greater for the cell without an MPL, which could not prevent accumulation of water at the cathode catalyst layer, leading to poor oxygen supply at the reaction sites.

Figure 11 shows the corresponding water crossover values measured at the anode. Again the two replicates showed good reproducibility with a maximum difference in water crossover flux of 1.74×10^{-7} $molcm^{-2}s^{-1}$ under the same conditions, equivalent to water generation at a current density of 34 $mAcm^{-2}$. Being the results of vapour phase diffusion only, the intercepts were clearly indicative of the RH gradients across the membrane for different runs: for cathode RH of 25% and anode RH of 75% at the inlets, water diffused

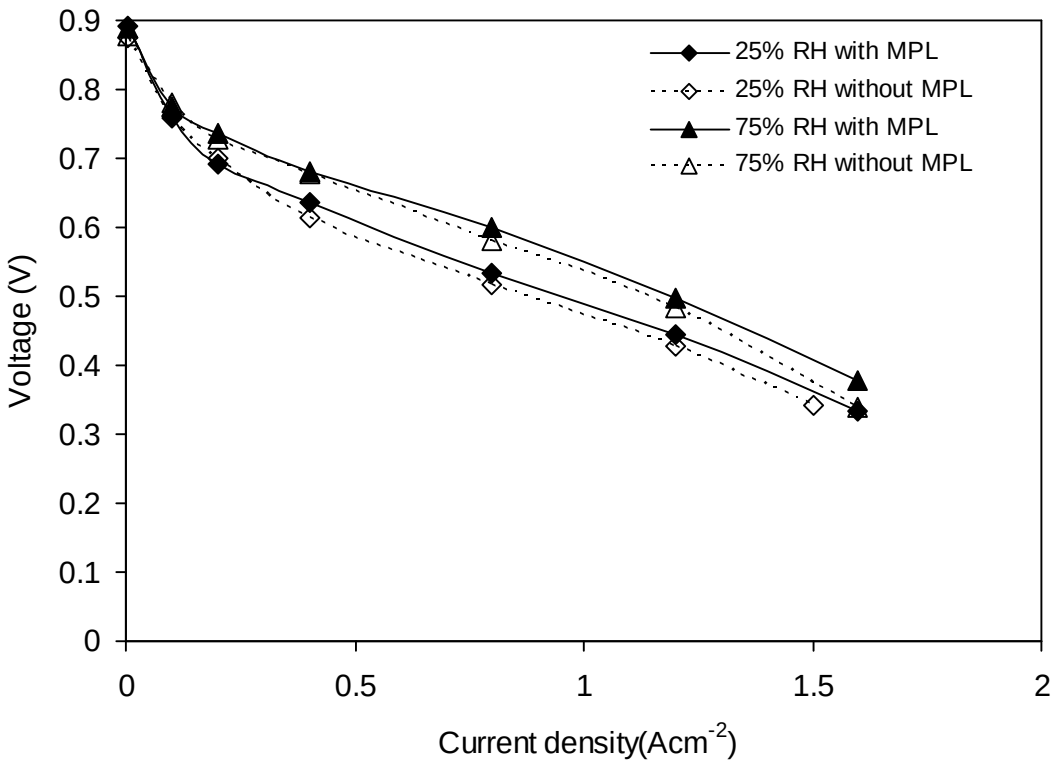

Figure 10. Experimental polarization curves at constant fuel and oxidant flow rates. Results are the average from two replicates. MEA construction and cathode RH are as indicated. T = 70 °C, P_A = 230 kPa, P_C = 230 kPa, $RH_{in,A}$ = 75%, H_2 flow rate = 4.46×10^{-3} $mols^{-1}$, N_2 flow rate = 2.94×10^{-3} $mols^{-1}$, O_2 flow rate = 7.81×10^{-4} $mols^{-1}$.

from anode to cathode yielding a positive water crossover flux. When there was no difference in the feed RH between the two sides of the membrane, no water crossover could be observed. A larger current density produced more water at the cathode catalyst layer and hence a greater diffusion gradient across the membrane, leading to more back diffusion and hence a decrease in water crossover fluxes. The trends in water crossover flux against current density were highly linear up to around 1.5 Acm^{-2} for 25% cathode RH and 1.2 Acm^{-2} for 75% cathode RH. The curve for 75% cathode RH slightly flattened out at high current densities. This is consistent with what was found in the previous chapter.

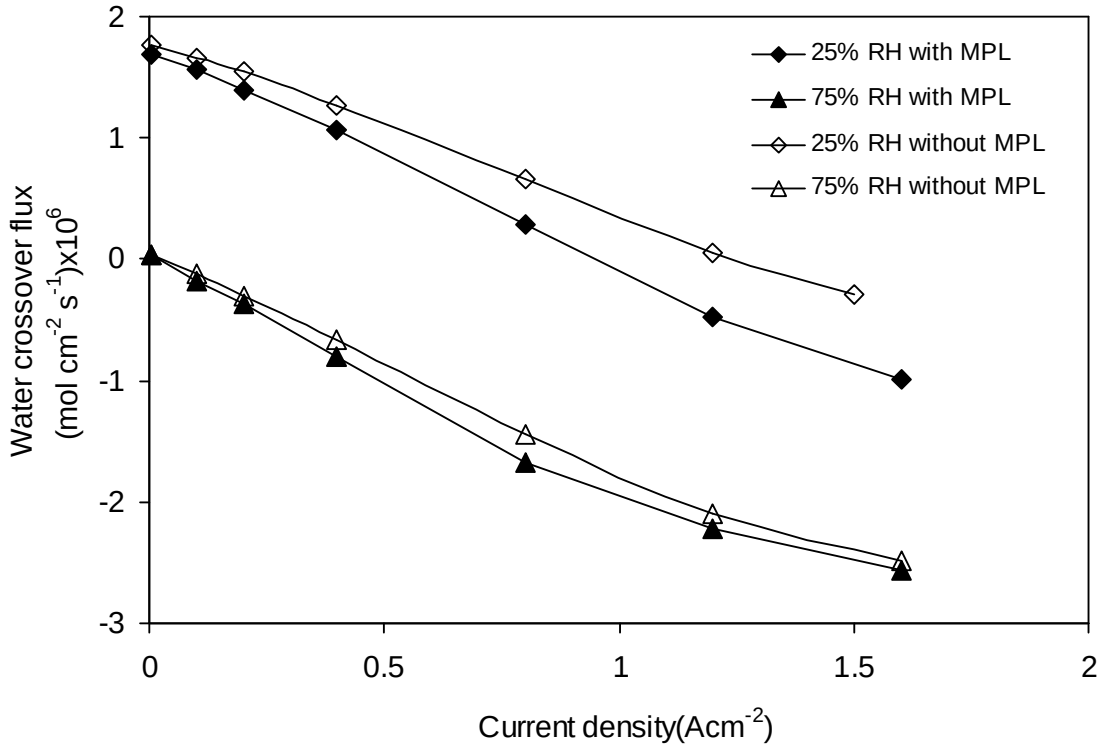

Figure 11. Water crossover flux (measured from anode) against current density. Negative values indicate water transfer from cathode back to anode. Results are the average from two replicates. MEA construction and cathode RH are as indicated. T = 70 °C, P_A = 230 kPa, P_C = 230 kPa, $RH_{in,A}$ = 75%, H_2 flow rate = 4.46×10^{-3} $mols^{-1}$, N_2 flow rate = 2.94×10^{-3} $mols^{-1}$, O_2 flow rate = 7.81×10^{-4} $mols^{-1}$.

By comparing the water crossover behaviour for MEAs with and without MPL, it could be seen that adding an MPL makes the slope of the curve more negative for 25% cathode RH. Therefore, the addition of MPL did enhance back diffusion of product water to the anode channel at 25% cathode RH. Using equation 28 to calculate generated water distribution, 27.4% of the water generated ended up in the anode channel without an MPL while that for the MEA with MPL would be 33.7%. However in the case of 75% cathode RH, the difference was a lot smaller. For the linear region up to 1.2 Acm^{-2}, 34.9% of the water generated was distributed to the anode without an MPL while the presence of MPL only increased this percentage to 37.4%. This was consistent with the findings by Atiyeh et al. (2007) that insignificant changes in water crossover occurred at anode and cathode humidities of 60% and 100%, respectively. In addition, this difference diminished at higher current densities, where the cathode was increasingly saturated. In

contrast, the results from Kim et al. (2010) showed that MPL on the cathode side enhanced water transfer back to the anode side when the cathode feed was saturated with water vapour.

A common explanation for the action of the MPL is that it decreases the equilibrium saturation vapour pressure by means of capillary action, which can be described by the Kelvin equation (Murahashi 2006, Kim 2010):

$$P_{sat} = P_{sat,fs} \exp\left(-\frac{2\tau V_m}{rRT}\right) \quad [32]$$

An MPL has a much smaller pore radius *r* compared to a carbon paper only GDL. From the above equation, using an MPL leads to a lower equilibrium saturation vapour pressure at the cathode membrane interface. The same water vapour pressure is now equivalent to a higher RH, thereby increasing the RH gradient across the two membrane- electrode interfaces and enhances diffusion of water back to the anode side. In theory this effect is present regardless of the current density. It follows that even under the same inlet humidity at both electrodes and no current is drawn, there would be a flow of water from the cathode to the anode upon the addition of an MPL. However as observed experimentally, the intercepts at 75% cathode RH were almost the same (close to zero water crossover) for the two different sets of MEAs (with and without MPL on the cathode side).

Another possibility for the role of the MPL is that it discourages the transport of water from the cathode membrane interface to the cathode channel, in effect decreasing the transport coefficient for water vapour there. As a result, more generated water has to move towards the anode side, leading to a more negative water crossover flux. When there is no RH gradient across anode and cathode channels and no load, any changes in transport resistance between the channels have no effect at all, which is consistent with our experimental findings. This model can also account for the MPL's diminishing effect on back diffusion enhancement at high cathode inlet RH. Consider a cathode catalyst layer of zero thickness, which essentially assumes that water is generated by the electrochemical reaction at the cathode membrane interface. Water desorption from the

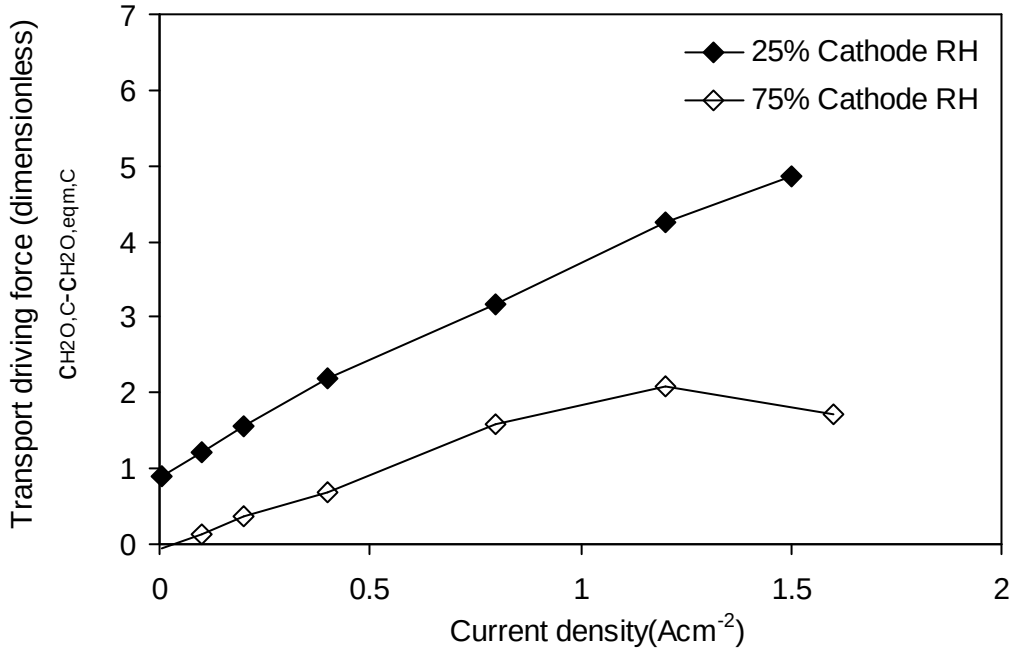

Figure 12. Driving force for water transport at the cathode membrane interface as predicted by the Berg model. The conditions for simulation are the same as for the experiments without an MPL.

membrane to the cathode channel is proportional to the difference between the water content at the cathode membrane interface and the equilibrium water content with the cathode channel humidity (Bird et al. 2007, Berg et al. 2004):

$$J_{H_2O,desorption} = -a\gamma_C\left(c_{H_2O,C} - c_{H_2O,eqm,C}\right) \quad [33]$$

When the cathode RH is high, the equilibrium water content at the interface $c_{H_2O,eqm,C}$ would also be high, according to Springer et al. (1991). Under the same current density, the water brought to the cathode membrane interface by electro-osmotic drag and generation from reaction would be the same, leading to similar water contents at that interface. Therefore the driving force, $c_{H_2O,C} - c_{H_2O,eqm,C}$, would decrease as a result of increasing cathode RH, as shown by the simulation using the Berg model in Figure 12. With a smaller driving force for water transport, water crossover would be less sensitive to the changes in the transport coefficient under high cathode RH. The effect of MPL in changing the transport behaviour at the cathode catalyst layer is thus reduced, which in

turn diminishes the difference in back diffusion and then the water crossover rate when inlet RH is high.

The explanatory powers of the two hypotheses described above were examined by independently incorporating each of these effects into the Berg model. For the capillary action model (CAM), the activity (RH) used in equation 29 in Berg et al. (2004) was given by

$$RH = \frac{P_{H_2O}}{P_{sat}(T)\exp\left(-\frac{2\tau V_m}{rRT}\right)} \qquad [34]$$

at the cathode side. The additional parameter brought by this correction was the pore radius r. On the other hand, for the transport reduction model (TRM), equations 31 in Berg et al. (2004) was simply replaced by equation 33 in this thesis. The additional parameter was the cathode desorption coefficient γ_C.

The experimental data for the MEA without MPL was used for curve fitting in order to obtain the best-fit parameters for the original Berg model. Both polarization and water crossover data were used, in accordance to a 'dual response' fitting (DRF) method which will be described in detail in Chapter 5. The two new corrected models were used to fit the data for the MEA with MPL, using the parameter set from the original model and tuning only the additional parameter (r for CAM, γ_C for TRM) using DRF. The best-fit pore radius in CAM was found to be 1.3×10^{-8} m, which was at the same order of magnitude as the pore size in typical microporous layers measured by mercury porosimetry (Park 2006, Owejan 2010). The best-fit cathode desorption coefficient in TRM was found to be 25.8% smaller than the original coefficient without an MPL. This was consistent with the assumption that the MPL discouraged the evolution of generated water to the cathode channel.

In Figure 13, a decent fit was obtained using the original model for the data without MPL. Both CAM and TRM could capture a voltage increase with the presence of an MPL. However, these effects were more significant at 25% cathode RH for TRM, while

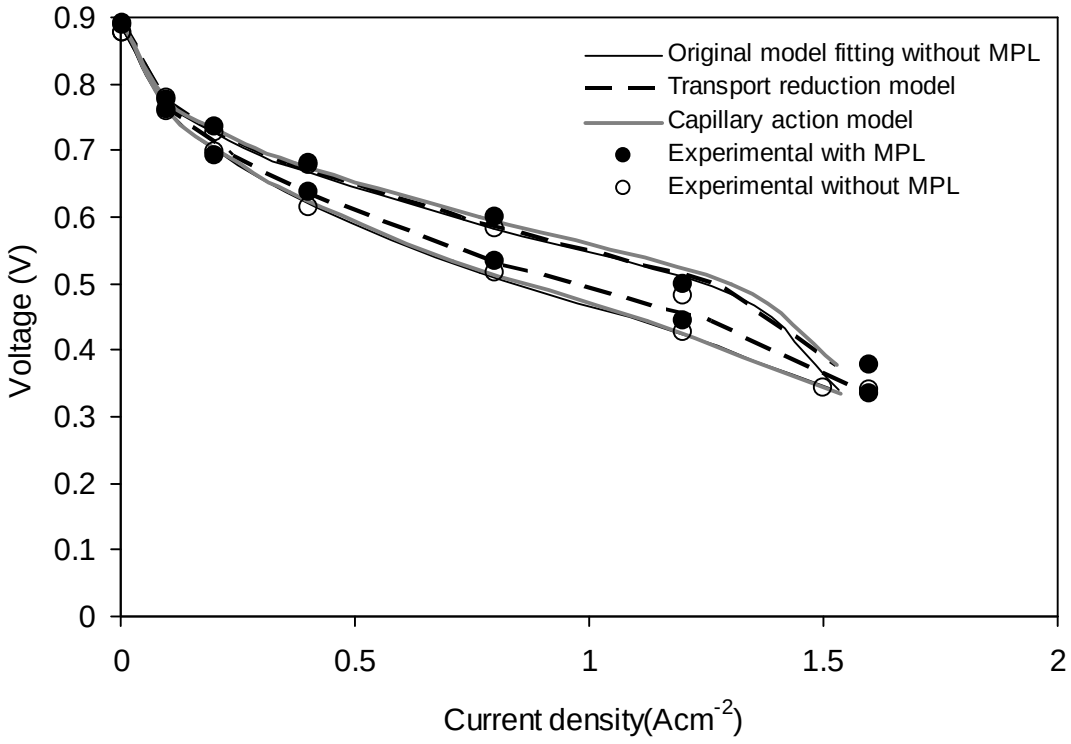

Figure 13. Fitting results on the polarization curves using different explanatory models for the action of the MPL. The original Berg model (solid black lines) was used to fit for data without MPL, the TRM (dotted lines) and CAM (solid grey lines) were used to fit the data with MPL.

CAM showed a larger increase in cell voltage at 75% cathode RH. In both models, the greater impact of inlet cathode humidity relative to the addition of an MPL on polarization was well preserved.

However the story was quite different for water crossover fittings. Figure 14 shows that it was possible to fit experimental data without MPL well using the original model. As discussed previously, even with the same inlet humidities at both electrodes and no water production, CAM predicted a negative water crossover flux (from cathode to anode) due to the increase in RH at the cathode membrane interface by capillary action. Despite a best-fit pore radius was used, CAM underestimated the effect of back diffusion enhancement under 25% cathode RH and overestimated it under 75% cathode RH. Correspondingly, due to the higher membrane water content, the CAM predicted that the increase in voltage upon the addition of an MPL was small at 25% cathode RH compared

to 75% cathode RH. From equation 34, the best-fit pore radius of 1.3×10^{-8} m led to an increase in RH at the cathode membrane interface by 6.9% due to capillary action. From Figure 15, a change in RH from 25% to 26.7% did not increase the equilibrium water content significantly. As a result, CAM could hardly capture the large increase in back diffusion at 25% cathode RH. On the other hand, TRM gave a better fit in water crossover. The change in slope of the water crossover- current density relationship at 25% cathode RH was more significant than what was predicted by CAM, while at 75% cathode RH TRM managed to show the diminished effect of MPL on water crossover. With the same degree of freedom, it was obvious that TRM was more capable of describing our experimental results compared to CAM.

The Berg model as well as TRM did not treat the diffusion of water vapour between the membrane interface and the channel independently, but incorporated it together with interfacial water transport at the membrane interface by a lumped transport coefficient γ. When an MPL was added to the cathode, the diffusional resistance from the cathode channel to the cathode membrane interface increased, due to the MPL's smaller pore size. The overall resistance in the transport circuit from the cathode channel to the membrane would also increase, leading to a smaller cathode desorption coefficient γ_C in TRM. Ye et al. (2007b) measured the water crossover coefficient using gas diffusion layers with different predetermined effective diffusivities. They found that a smaller diffusivity yielded a lower water crossover coefficient, consistent with our arguments.

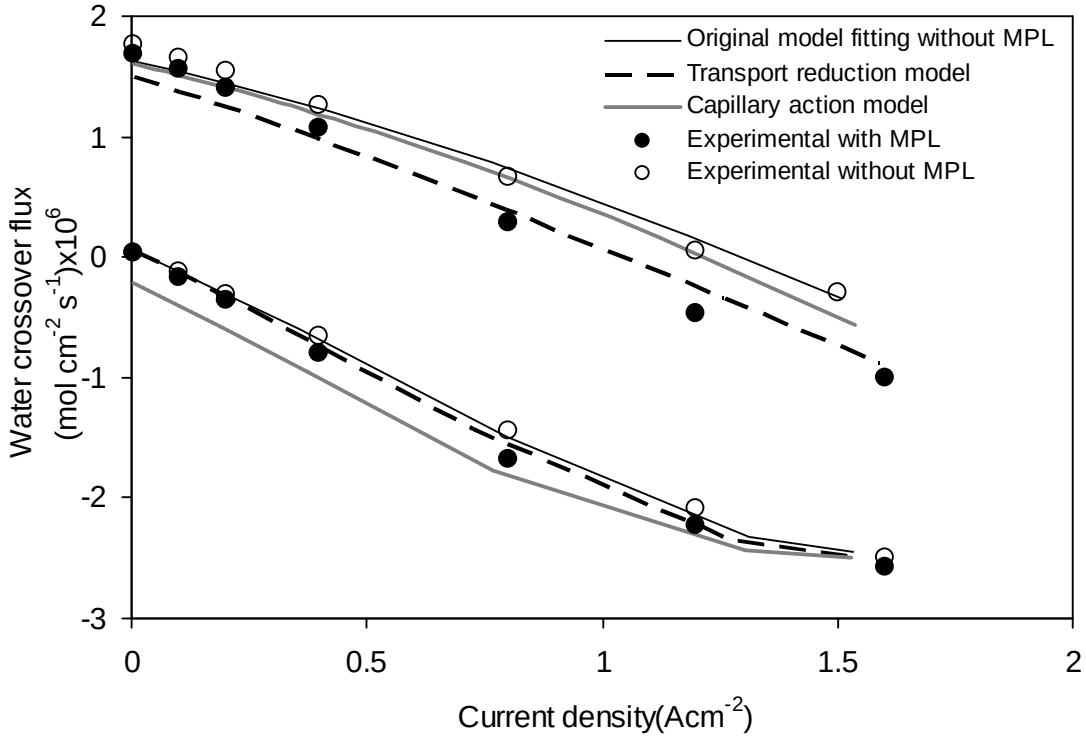

Figure 14. Fitting results on water crossover using different explanatory models for the action of the MPL. The original Berg model (solid black lines) was used to fit for data without MPL, the TRM (dotted lines) and CAM (solid grey lines) were used to fit the data with MPL.

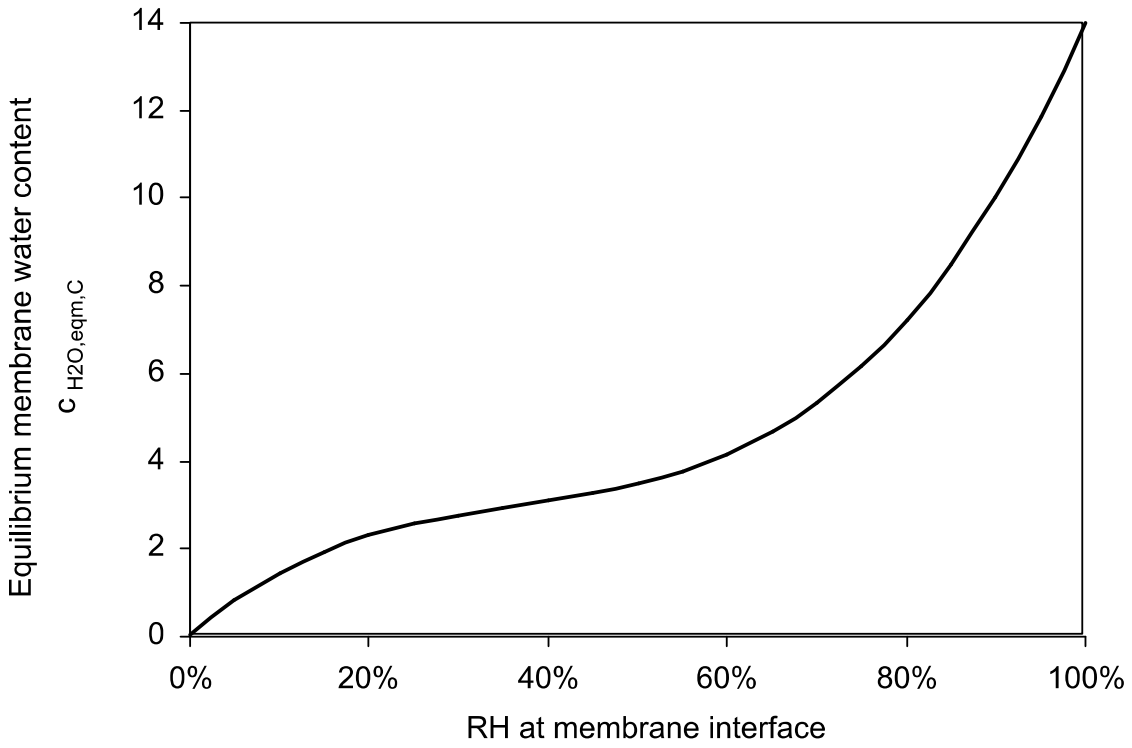

Figure 15. Relationship between equilibrium membrane water content and RH at the membrane interface predicted from the empirical fitting of experimental results (equation 16 in Springer et al. (1991)).

4.3. Roundup

The effect of an MPL on the cathode side of a PEM fuel cell on polarization and water crossover was examined experimentally with sub-saturated feeds. Adding an MPL increased the voltage under the same current density, but its effect was not as significant when compared to an inlet cathode RH increase from 25% to 75%. The water crossover flux decreased with the increase in current densities, while the curve slightly flattened under high current densities. This was due to a high degree of saturation at the cathode membrane interface. The cathode MPL increased back diffusion of water to the anode channel and hence a lower water crossover flux. However, this effect was much less significant when the inlet cathode RH was 75% and the effect was further diminished at high current densities. It was proposed that the MPL increased the transport resistance from the cathode channel to the cathode membrane interface, forcing more water to back diffuse to the anode side. Under high cathode RH, the driving force for water evolution to the cathode side was much smaller and therefore weakened the effects of the MPL on transport reduction. After verification using a mechanistic model by Berg et al. (2004), it was found that this hypothesis explained well the experimental results at high cathode RH, compared to the conventional capillary action model.

5. Use of Water Crossover Data in Parameter Estimation in PEMFCs

When studying water management in fuel cells quantitatively, the values of fuel cell parameters have to be obtained. These parameters could be used in various models to predict and control the behaviour of the fuel cell. Ex-situ experiments to measure water management related parameters have been described in Chapter 1.

On the other hand, curve fitting by appropriate models is an alternative technique in obtaining parameters for fuel cells. This is useful when such quantities are difficult or impossible to obtain directly from experiments due to coupling effects. Tao et al. (2006) gave a good review on the work done on these efforts. To achieve good accuracy in the parameters obtained, there have been some discussions on complementing the global polarization curve in validating or fitting fuel cell models. Berg et al. (2004) used the sum of squared residuals (SSR) of local current densities as the basis of fitting and parameter estimation. Ju and Wang (2004) suggested the use of current density distribution for the validation of their CFD model. Min et al. (2006) proposed the use of cathode overpotential on top of current density distribution and the polarization curve. However all the above approaches require special setups to provide the required experimental data. To obtain cathode overpotential data, one has to insert a reference electrode into the membrane as suggested by Han et al. (2003), while segmented current collectors are necessary for measuring the current density distribution (Stumper et al. 1998, Mench et al. 2003b). Alternatively, measuring the water content coming out from the electrodes is practised by a number of researchers using a wide variety of techniques, with no special modifications on the cell itself. Within the different methods reviewed previously, mass spectroscopy gas analyzers and infrared gas analyzers allow quick in-situ measurements of water crossover and hence provide a better picture of the relations between water crossover and operating conditions. Therefore using water crossover data in model validation and parameter fitting would be a more flexible methodology when used on a variety of cell designs. In addition, transport processes play a dominant role in water

crossover and hence it gives a more comprehensive picture of the fuel cell than relying on current density (and current density distribution) alone.

In this chapter, the use of experimental water crossover data in validating mechanistic models and estimating model parameters would be illustrated, using the Berg model as an example.

5.1. Parameter Fitting Procedures

After the acquisition of experimental data, the results from runs 1 to 5 in Chapter 3 were used to obtain parameters in the Berg model.

To obtain the four fitting parameters of the Berg model, two different approaches were used. The first one was the usual 'current density only' fitting (CDF), which minimizes the sum of squared residuals (SSR) in overall current density $\sum_i \left(\Delta \overline{I}_i\right)^2$ where $\Delta \overline{I}_i = \overline{I}_{model,i} - \overline{I}_{experimental,i}$ is the residual for the current density of the *i*-th data point. The minimization of the SSR was achieved by changing the values of the fitting parameters. The other one was to use both residuals in current density and water crossover flux data as an objective function to be minimized (later termed as 'dual response' fitting, DRF). Only the experimental water crossover flux data as determined from anode side measurements was used. The determinant criterion is a common objective function for multi-response regression, in which the determinant

$$\begin{vmatrix} \sum_i \left(\Delta \overline{I}_i\right)^2 & \sum_i \left(\Delta \overline{I}_i\right)\left(\Delta \overline{J}_{H_2O,i}\right) \\ \sum_i \left(\Delta \overline{I}_i\right)\left(\Delta \overline{J}_{H_2O,i}\right) & \sum_i \left(\Delta \overline{J}_{H_2O,i}\right)^2 \end{vmatrix} \qquad [35]$$

is minimized, where $\Delta \overline{J}_{H_2O,i} = \overline{J}_{H_2O,model,i} - \overline{J}_{H_2O,experimental,i}$ is the residual for the water crossover of the *i*-th data point (Beers 2007). However, for one of our curves, minimizing the above determinant did not give a decent fit to both current density and water crossover flux. It was suspected that the diagonal terms cancelled out each other to yield a misleading result. Oxby's objective function eliminated this problem as only the

product $\left(\sum_i \left(\Delta \overline{I}_i\right)^2\right)\left(\sum_i \left(\Delta \overline{J}_{H_2O,i}\right)^2\right)$ is used (Oxby 1997). It was shown by simulation experiments that this method was also suitable even if the measurement errors in current density and water crossover flux were correlated (Oxby 1997).

To assess the ability to give accurate estimates of the parameters, the 90% confidence intervals (marginal 90% highest posterior density intervals) were calculated for both CDF and DRF fitting. The formulae leading to these intervals are given in the appendix.

A gradient descent approach was used to find the minimum of the objective functions listed above, subject to upper and lower bounds of 1/25 and 25 times of the corresponding value published by Berg et al. (2004) As the initial guess of the parameters may lead to different fitted parameter values, it was desired to use a number of starting points as initial estimates. For each parameter, 1/5, 1 and 5 times of the values in Berg et al. (2004) were used as initial guesses, which made a total of 81 minimization runs. This was very computationally expensive, and an approximation was employed in the Berg model in the search of optimal fitting parameters. Equation 48 in Berg et al. (2004) was replaced by

$$\sigma = \left(\frac{RT}{aF^2} \frac{L_m}{D'_+ \left(c'_{H_2O}\right) c'_+} \right)^{-1} \qquad [36]$$

where c'_{H_2O} was the water content at the mid point of the membrane and D'_+ and c'_+ were the corresponding proton diffusivity and proton concentration at that point, respectively. This was essentially approximating the resistance profile along the thickness of the membrane as linear. It is shown later in this article that this was a reasonable approximation. Due to the stiffness of the equations which varied significantly depending on the model parameters used, an implicit integrator (Matlab's ODE15s) was adopted; while more robust, it yielded satisfactory results with a tenfold speed increase over an explicit integrator (Matlab's ODE45).

5.2. Results and Discussion

Figure 16 shows the simulated membrane resistance profile for run 1 in the full scale model using the best 'dual parameter' fitted parameters. The high linearity assured the accuracy of the linear approximation of equation 36. A thin membrane minimized differences between local and global water contents gradients and hence made water content and resistance profiles linear. In all cases the resistance decreases from anode to cathode, which was expected as the cathode had higher local water content. Compared to Watanabe et al. (1998), who used almost dry gas feeds and a thicker membrane of 60 microns, the shape of the resistance profile was less dependent on current density in our

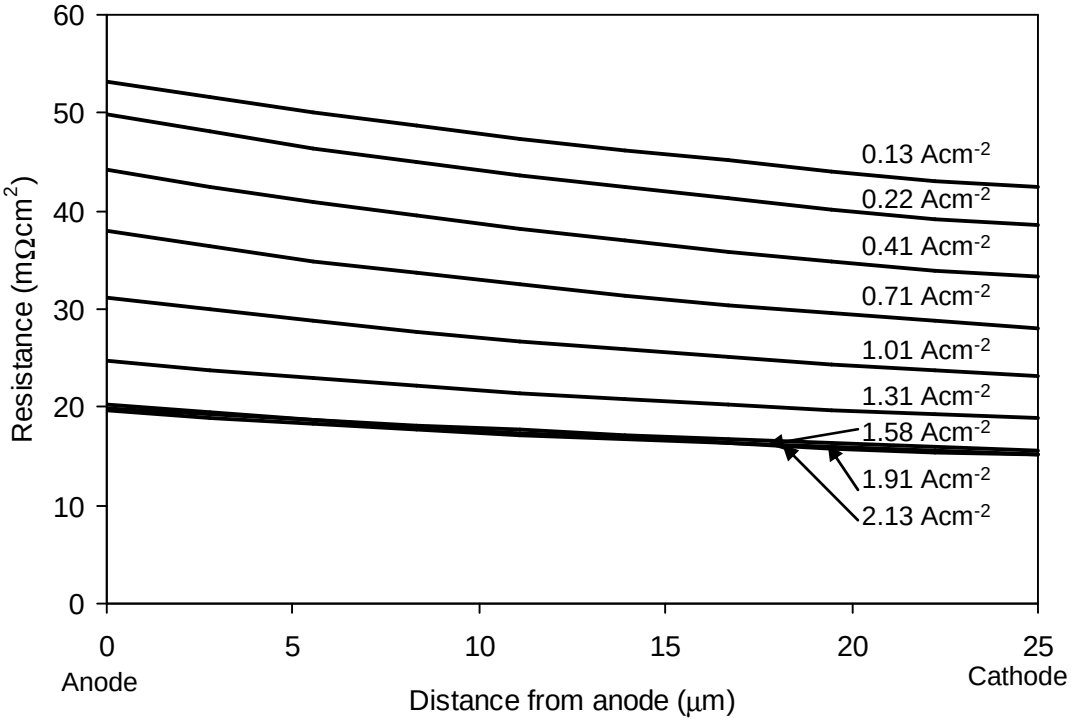

Figure 16. Membrane resistance profile along the membrane thickness direction, obtained by the 'full scale' Berg model for run 1 (T = 60 °C, P_A = 230 kPa, P_C = 200 kPa, $RH_{in,A}$ = 25%, $RH_{in,C}$ = 75%. H_2 flow rate = 3.13×10^{-3} mols^{-1}, N_2 flow rate = 2.98×10^{-3} mols^{-1}, O_2 flow rate = 7.46×10^{-4} mols^{-1}) and its corresponding 'best fit' parameters from DRF. The left side of the graph represents the anode catalyst layer interface of the membrane while the right side represents the cathode catalyst layer interface. From the top to the bottom the current density is increasing, leading to increasing water generation, membrane hydration and decreasing resistance.

simulation. This was because in our experiments the RH gradient between cathode and anode already provided some degree of hydration at low current densities. Using the same set of parameters, the difference between the simplified and full scale Berg model is shown in Figure 17 and Figure 18. A very close fit in both current density and water crossover flux was found.

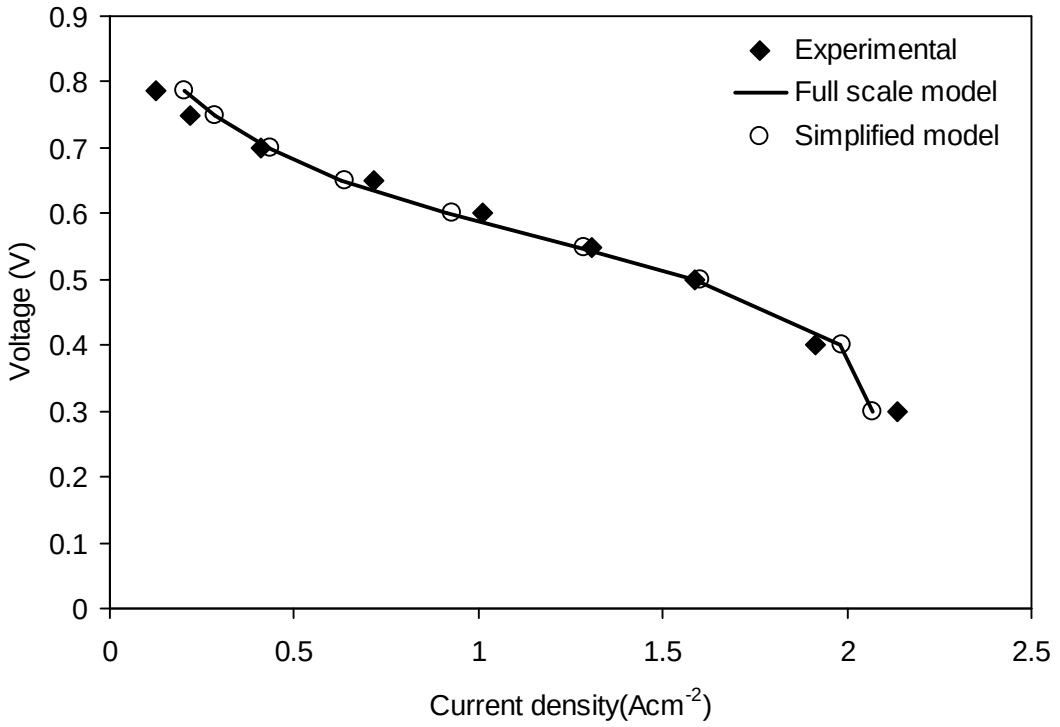

Figure 17. The difference between experimental polarization curve, 'full scale' Berg model and simplified Berg model predictions for run 1 (T = 60 °C, P_A = 230 kPa, P_C = 200 kPa, $RH_{in,A}$ = 25%, $RH_{in,C}$ = 75%. H_2 flow rate = 3.13×10^{-3} $mols^{-1}$, N_2 flow rate = 2.98×10^{-3} $mols^{-1}$, O_2 flow rate = 7.46×10^{-4} $mols^{-1}$), using the corresponding 'best fit' parameters from DRF.

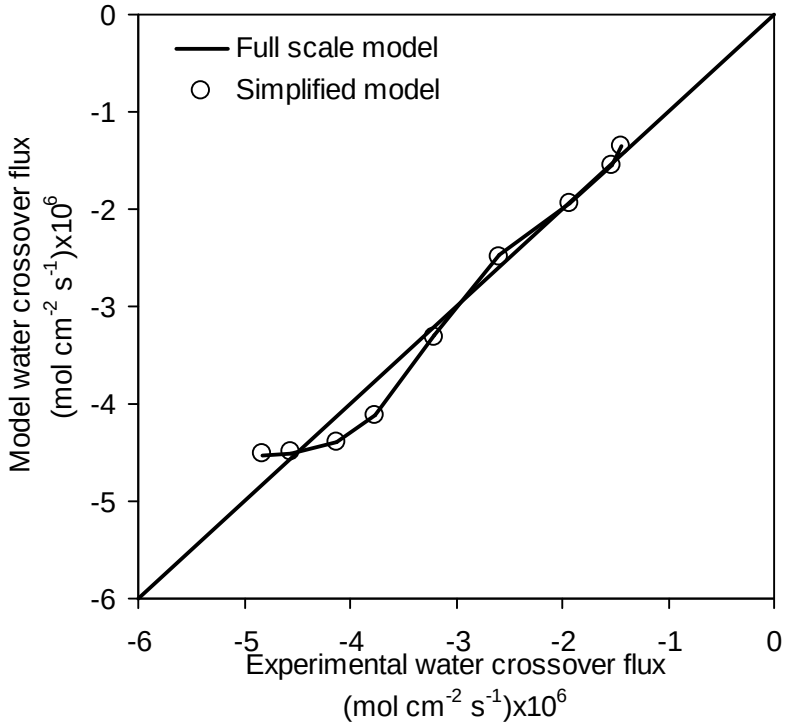

Figure 18. The difference between measured and predicted water crossover fluxes for the 'full scale' Berg model and simplified Berg model predictions for run 1 (T = 60 °C, P_A = 230 kPa, P_C = 200 kPa, $RH_{in,A}$ = 25%, $RH_{in,C}$ = 75%. H_2 flow rate = 3.13×10^{-3} $mols^{-1}$, N_2 flow rate = 2.98×10^{-3} $mols^{-1}$, O_2 flow rate = 7.46×10^{-4} $mols^{-1}$), using the corresponding 'best fit' parameters from DRF. The solid diagonal line is the x=y curve which acts as a rule to determine the deviation of model predicted water crossover flux from the experimentally obtained values.

As described in the previous section, 81 different starting points were used to find the 'global fit'. It was found that different choices of starting values yielded 3 distinct local minima for the sum of squared residuals in current density. Because some of the parameter values can vary in orders of magnitude in literature (see Ge et al. (2005) for the ranges of γ obtained by different groups as an example), one has to be cautious in employing literature values as starting points for parameter fitting so as not to fall into the 'false' local minima and obtained 'false' best fit parameters. Fortunately, the best fitted parameters converged to some point for trials resulting in the smallest local minima. It was highly likely that there existed a unique set of parameters which led to an absolute minimum within the relatively broad range (25 times difference between maximum and minimum for each parameter) considered, although there was no guarantee that the 81

starting points covered all possible troughs in the objective function- parameter space. The fitting results thus obtained would be reliable for model validation because the best the Berg model could predict was already reflected by them. The same approach would be employed for all the fits discussed later in this article.

For the sake of accuracy, the 'full scale' model was used for all results discussed below in this article unless otherwise specified. Figure 19 shows the CDF and DRF fits for each of the runs respectively. In Figure 19, CDF did a good job in the polarization curve for individual runs, while DRF over estimated the current at the kinetic limited zone and underestimated it at the transport limited zone. On the other hand, from Figure 20, CDF heavily overestimated water crossover flux at both ends of the polarization curve, i.e. the effect of back diffusion was underestimated, while DRF gave a better result. This

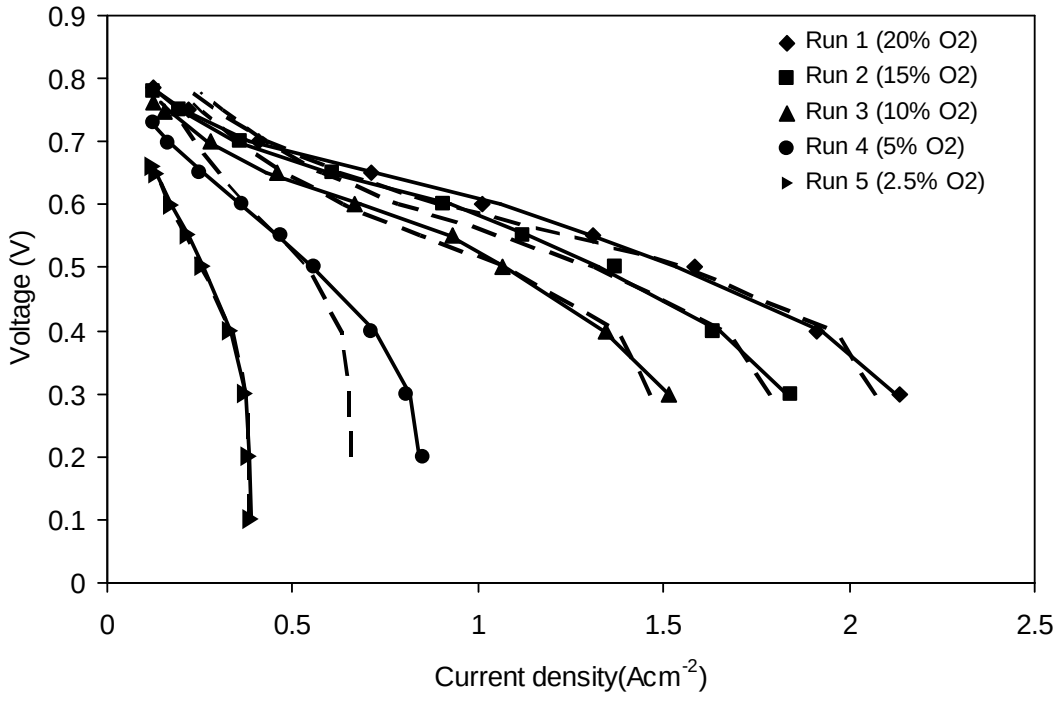

Figure 19. Comparison between experimental polarization curves and model 'best fit' values fitting runs 1 to 5 individually. Symbols: experimental results; solid lines: CDF results; dashed lines: DRF results. O_2 concentrations on the cathode are as indicated. T = 60 °C, P_A= 230 kPa, P_C = 200 kPa, $RH_{in,A}$ = 25%, $RH_{in,C}$ = 75%, H_2 flow rate = 3.13×10^{-3} $mols^{-1}$, N_2 and O_2 total flow rate = 3.73×10^{-3} $mols^{-1}$.

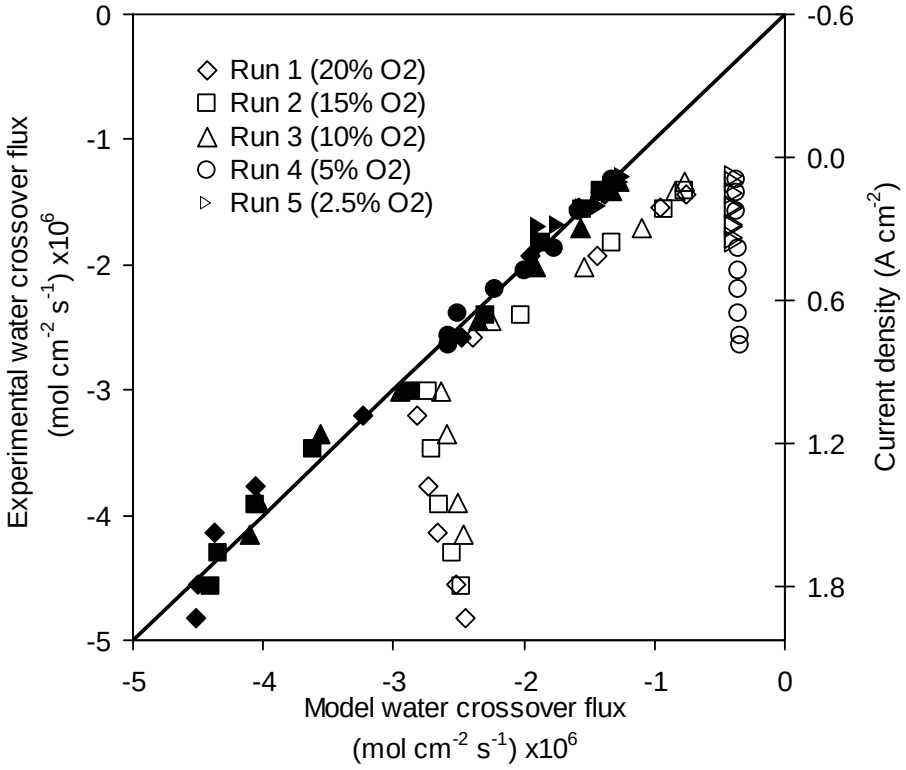

Figure 20. Comparison between experimental water crossover flux and model 'best fit' values fitting runs 1 to 5 individually. Solid symbols: DRF results; hollow symbols: CDF results. Axis on the right is the corresponding current density in Acm^{-2} for that particular value of experimental water crossover flux, utilizing the observed linear relationship between them (Figure 4). O_2 concentrations on the cathode are as indicated. T = 60 °C, P_A= 230 kPa, P_C = 200 kPa, $RH_{in,A}$ = 25%, $RH_{in,C}$ = 75%, H_2 flow rate = 3.13×10^{-3} $mols^{-1}$, N_2 and O_2 total flow rate = 3.73×10^{-3} $mols^{-1}$.

somehow exposed the weakness of the Berg model in predicting water crossover, especially at current densities of <0.4 Acm^{-2} and >1 Acm^{-2}. At high current densities, CDF gave slightly higher water crossover flux values. It was likely that at this range, the model treated the membrane as fully saturated and so virtually no further back diffusion could occur, forcing the water produced from the oxygen reduction reaction to the cathode channel and increasing the water crossover flux. In the model the maximum water content was assumed to be the vapour equilibrated maximum of 14 rather than the liquid equilibrated maximum of 21 (Zawodzinski et al. 1993b). As a result, the water content gradient and back diffusion reached constant values too early. Similar trends were observed when all the five runs were fitted together (all-at-once fit), as suggested by Figure 21 and Figure 22.

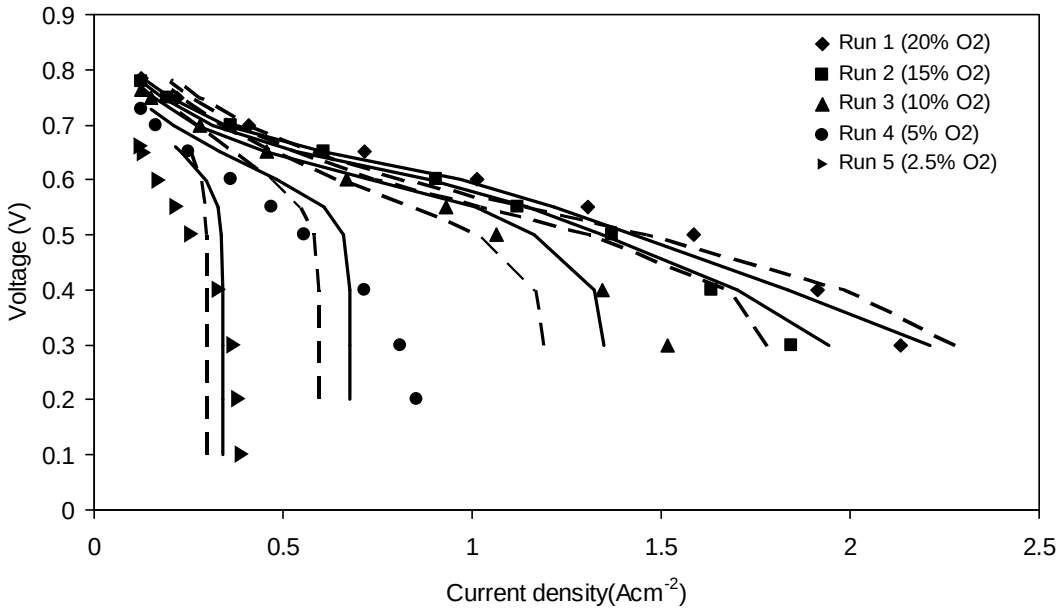

Figure 21. Comparison between experimental polarization curves and model 'best fit' values fitting runs 1 to 5 all-at-once. Symbols: experimental results; solid lines: CDF results; dashed lines: DRF results. O_2 concentrations on the cathode are as indicated. T = 60 °C, P_A = 230 kPa, P_C = 200 kPa, $RH_{in,A}$ = 25%, $RH_{in,C}$ = 75%, H_2 flow rate = 3.13×10^{-3} $mols^{-1}$, N_2 and O_2 total flow rate = 3.73×10^{-3} $mols^{-1}$.

Table 3 listed the corresponding residuals for current density and water crossover flux, respectively, using the full scale model with parameters obtained by the simplified model. In general, while CDF gave a better fit for the polarization curve with SSRs one order of magnitude smaller. DRF gave a better fit for water crossover flux with SSRs two orders of magnitude smaller. The overall 'goodness of fit' for both quantities was defined simply as the objective function used by Oxby, $\left(\sum_i \left(\Delta \overline{I}_i\right)^2\right)\left(\sum_i \left(\Delta \overline{J}_{H_2O,i}\right)^2\right)$ (Oxby 1997). Specifically fitted to minimize this product, DRF gave an order of magnitude better results. As one would expect, the SSRs for the all-at-once fit would be larger than the sum of the SSRs for individual fits. As shown in Table 3, for CDF, the all-at-once fit had SSRs in current density of 0.295 A^2cm^{-4}, an order of magnitude greater than summing up the SSRs for individual fits, which was 0.0126 A^2cm^{-4}. For DRF, a 3 times increase was observed (0.623 A^2cm^{-4} versus 0.235 A^2cm^{-4}). For water crossover flux, surprisingly, the all-at-once 'current density fit' gave a smaller SSR compared to the sum

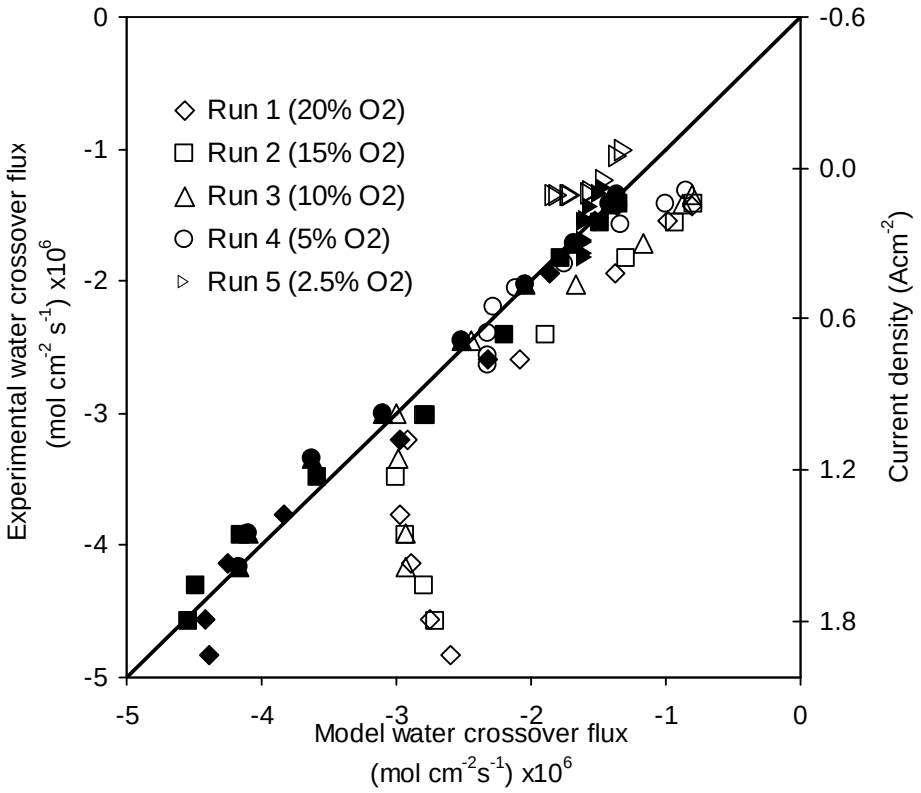

Figure 22. Comparison between experimental water crossover flux and model 'best fit' values fitting runs 1 to 5 all-at-once. Solid symbols: DRF results; hollow symbols: CDF results. Axis on the right is the corresponding current density in A/cm^2 for that particular value of experimental water crossover flux, utilizing the observed linear relationship between them (Figure 4). O_2 concentrations on the cathode are as indicated. T = 60 °C, P_A = 230 kPa, P_C = 200 kPa, $RH_{in,A}$ = 25%, $RH_{in,C}$ = 75%, H_2 flow rate = 3.13×10^{-3} mols^{-1}, N_2 and O_2 total flow rate = 3.73×10^{-3} mols^{-1}.

of the SSRs for individual fits (2.554×10^{-11} mol^{2}cm^{-4}s^{-2} versus 7.224×10^{-11} mol^{2}cm^{-4}s^{-2}); while the all-at-once SSR doubled the sum of individual SSRs when the 'DRF' approach was used (1.13×10^{-12} mol^{2}cm^{-4}s^{-2} versus 6.00×10^{-13} mol^{2}cm^{-4}s^{-2}).

The above findings pointed out the importance of using experimental results in addition to the polarization curve for parameter estimation and model validation. The polarization curve data alone are not comprehensive enough to provide an overall picture in the fuel cell and can lead to inaccuracies in the parameters thus obtained. With the help of DRF, the inaccuracies between the two responses are compromised to give more sensible predictions, when one is to accept these predictions by a specific model.

Table 3. The values of various goodness of fit quantities resulted from the parameters listed in Table 4. In the first five columns, the curves were fitted individually (from run 5 to run 1). In the sixth column, runs 1 to 5 were fitted all-at-once. In the seventh column, the residuals from model predictions using the parameters obtained from run 1 were presented.

		O_2 concentration (%)					All-at-	
		2.5	5	10	15	20	once	Run 6
SSR $\sum_i \left(\Delta \bar{I}_i\right)^2$	CDF	0.038	0.611	1.899	3.882	6.127	294.73	47.7
$(A^2cm^{-4}) \times 10^3$	DRF	0.172	84.522	42.320	62.030	46.020	623.67	235
Average SSR $\frac{1}{N}\sum_i \left(\Delta \bar{I}_i\right)^2$	CDF	0.004	0.068	0.211	0.431	0.681	6.550	5.300
$(A^2cm^{-4}) \times 10^3$	DRF	0.019	9.391	4.702	6.892	5.113	13.859	26.111
SSR $\sum_i \left(\Delta \bar{J}_{H_2O,i}\right)^2$	CDF	1.330	2.656	0.692	1.105	1.441	2.554	0.494
$(mol^2cm^{-4}s^{-2}) \times 10^{11}$	DRF	0.008	0.003	0.012	0.011	0.026	0.113	0.219
Average SSR $\frac{1}{N}\sum_i \left(\Delta \bar{J}_{H_2O,i}\right)^2$	CDF	0.148	0.295	0.077	0.123	0.160	0.057	0.055
$(mol^2cm^{-4}s^{-2}) \times 10^{11}$	DRF	0.001	0.0003	0.001	0.001	0.003	0.003	0.0243
Product of SSRs $\left(\sum_i \left(\Delta \bar{I}_i\right)^2\right)\left(\sum_i \left(\Delta \bar{J}_{H_2O,i}\right)^2\right)$	CDF	0.051	1.622	1.313	4.289	8.826	752.76	23.563
$(A^2\ mol^2cm^{-8}s^{-2}) \times 10^{14}$	DRF	0.001	0.233	0.501	0.670	1.189	70.015	51.563
Product of average SSRs $\frac{1}{N^2}\left(\sum_i \left(\Delta \bar{I}_i\right)^2\right)\left(\sum_i \left(\Delta \bar{J}_{H_2O,i}\right)^2\right)$	CDF	0.0006	0.0200	0.0162	0.0530	0.1090	0.3717	0.291
$(A^2\ mol^2cm^{-8}s^{-2}) \times 10^{14}$	DRF	0.00001	0.0029	0.0062	0.0083	0.0147	0.0346	0.637

The trends in the best fitted model parameters are shown in Figure 23 as a function of O_2 concentration. While there were no significant changes for DRF, a distinct jump in the membrane interfacial water transfer coefficient was observed for CDF fit when oxygen changed from 5% to 10%. DRF best fitted values were much closer to the γ value of $(9.89\pm0.91)\times10^{-6}$ ms^{-1}, estimated in the previous section, than the CDF counterparts. From Figure 23 (b), no great difference in oxygen diffusivity factor δ was found by using

the two fitting methods. Both showed a general increasing trend, which was equivalent to decreasing effective oxygen diffusivities. The increase in local liquid water content at the catalyst layer could be a possible reason, which was not considered in the model. The general agreement of values between the two fitting approaches implied that this parameter had little correlations with water crossover flux estimation. The variation in the results in the exchange current density $i_{o,c}$ was over an order of magnitude (Figure 23 (c)) and no distinct trend can be observed which could be due to the lack of data points in the kinetic region of the polarization curves. Consequently, the results are consistent with an ORR reaction order of one (see equation 25 in Berg et al. (2004)) The effective membrane conductivity σ was defined as the conductivity at full humidification (c_w = 14), while its inverse was the effective membrane resistivity. The values of effective membrane resistance obtained from CDF and DRF were not significantly different except at low oxygen concentrations, as illustrated in Figure 23 (d). As the oxygen concentration increased, more water was produced and the model may not be adequate to capture correctly the increased water content in the membrane, leading to decreasing effective membrane resistance.

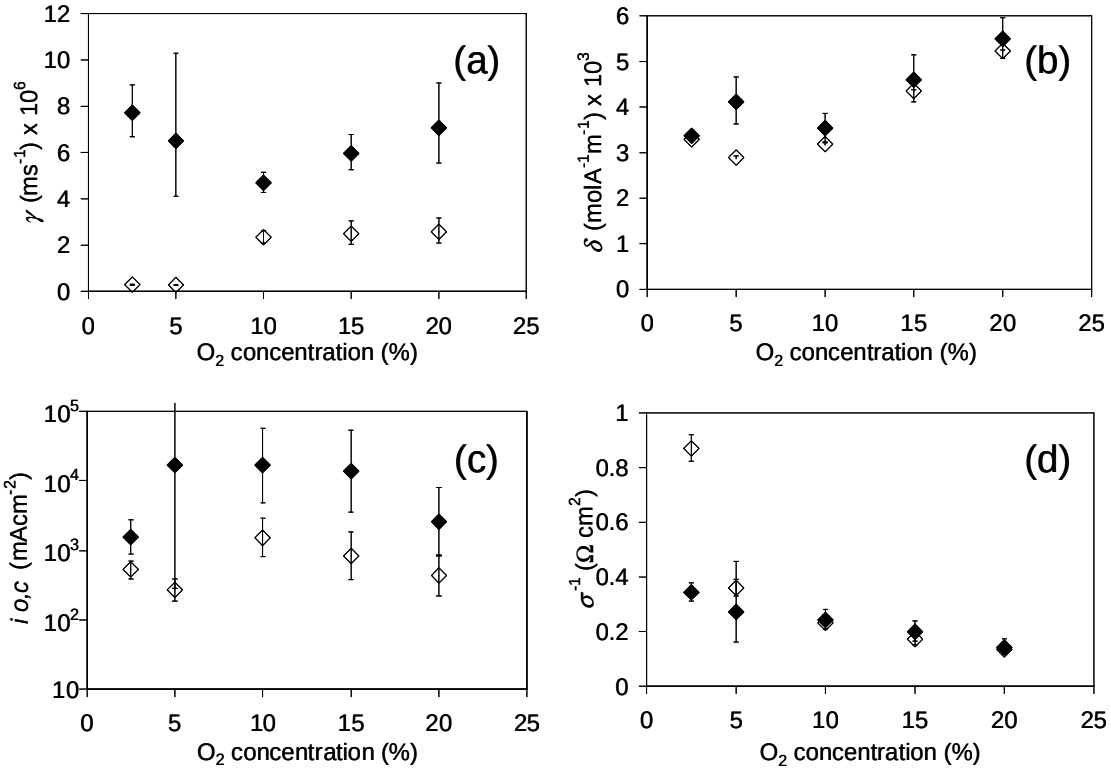

Figure 23. The 'best fit' values of (a) membrane interfacial water transfer coefficient γ; (b) oxygen diffusivity factor δ; (c) exchange current density $i_{o,c}$; (d) effective membrane resistance σ^{-1} individually for runs 1 to 5, plotted against the corresponding oxygen concentrations in these runs. Solid symbols represent DRF while hollow symbols represent CDF. Error bars indicate the confidence intervals for the parameter. Refer to Table 4 for the corresponding parameters for all-at-once fitting.

Araki et al. (2005) measured the resistance of membrane electrode assemblies humidified by 100% RH gases. To eliminate the effect of different membrane thickness and temperature in their experiments, the corresponding resistance was estimated using the relationship derived from Equation 48 in Berg et al. (2004)

$$\frac{1}{\sigma} \propto \frac{L_m T}{\exp\left(-\frac{1683}{T}\right)} \qquad [37]$$

as a comparison. Our results at 20% O_2 concentration (0.14 Ω cm^2) agreed well with the value of 0.15 Ω cm^2 obtained by Araki et al. (2005), though being an order of magnitude

Table 4. Parameters obtained from the best CDF and DRF from 81 starting points. The relative errors are defined by equation 38 (CDF) and equation 40 (DRF). For O_2 concentrations from 2.5% to 20%, the curves were fitted individually (from run 5 to run 1). In last 2 rows, runs 1 to 5 were fitted all-at-once.

		Value				Relative error			
O_2 conc. (%)		γ (ms^{-1}) $\times 10^6$	δ ($molA^{-1}\,m^{-1}$) $\times 10^3$	$i_{o,c}$ ($mAcm^{-2}$)	σ^{-1} ($\Omega\ cm^2$)	γ	δ	$i_{o,c}$	σ^{-1}
2.5	CDF	0.29	3.29	142	0.87	8%	1.00%	46%	6%
	DRF	7.72	3.37	550	0.34	15%	2%	101%	10%
5	CDF	0.28	2.89	62	0.36	0%	3%	58%	9%
	DRF	6.51	4.11	10643	0.27	58%	13%	15854%	68%
10	CDF	2.35	3.19	538	0.23	12%	7%	122%	11%
	DRF	4.70	3.54	10641	0.24	10%	9%	371%	16%
15	CDF	2.49	4.35	255	0.17	23%	6%	168%	14%
	DRF	5.97	4.60	8432	0.20	13%	12%	444%	20%
20	CDF	2.58	5.23	112	0.14	23%	5%	134%	14%
	DRF	7.07	5.49	1031	0.14	27%	8%	314%	22%
All-at-once	CDF	2.81	3.94	210	0.17	14%	7%	16%	7%
	DRF	6.77	4.64	1462	0.16	10%	5%	164%	14%

larger than the corresponding value of 17mΩ cm^2 from Ye and Wang (2007a) and the value by Berg et al. (2004) was 40% smaller at 80mΩ cm^2.

Figure 24 shows the model prediction results for run 6; using parameters obtained from the best CDF and DRF fittings of run 1. The only difference between runs 1 and 6 was the RH, with 25% anode/ 75% cathode in run 1 and 75% anode/ 25% cathode in run 6. CDF gave a reasonable prediction on current density, while DRF slightly underestimated the ohmic resistance region. For water crossover flux, DRF gave a closer prediction, with a SSR 50% smaller. This reflected the complexity in modelling water management issues by a specific model, and care has to be taken in the analysis of the predicted results.

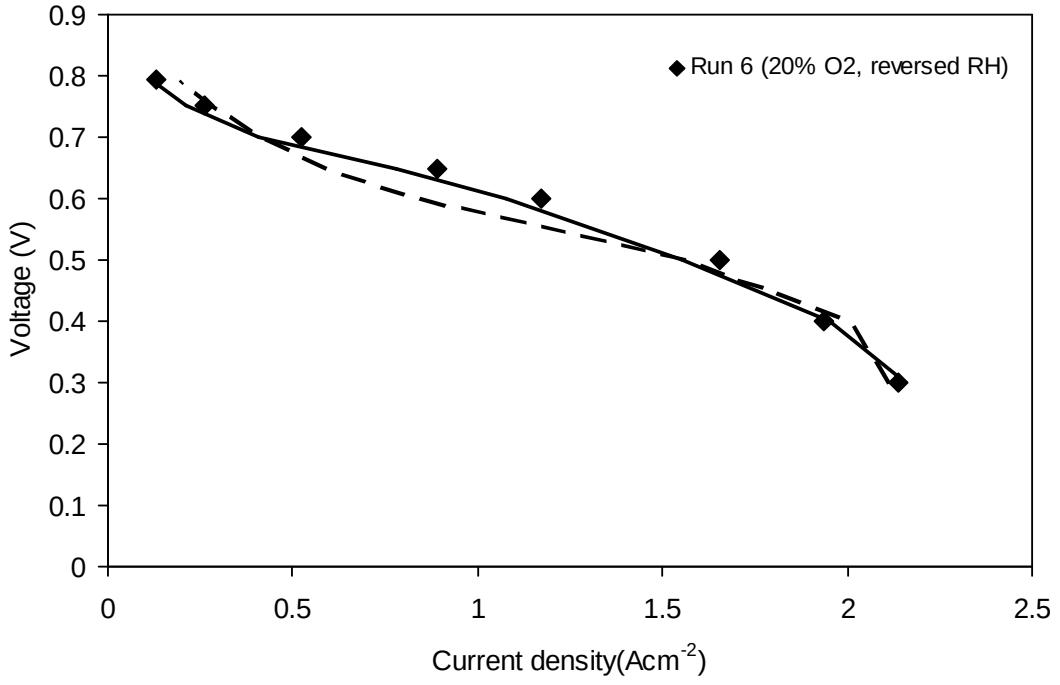

Figure 24. Comparison between experimental polarization curves and model predictions on run 6 from 'best fit' values fitting run 1. Symbols: experimental results; solid lines: CDF results; dashed lines: DRF results. T = 60 °C, P_A= 230 kPa, P_C = 200 kPa, $RH_{in,A}$ = 75%, $RH_{in,C}$ = 25%, H_2 flow rate = 3.13×10^{-3} mols^{-1}, N_2 flow rate = 2.98×10^{-3} mols^{-1}, O_2 flow rate = 7.46×10^{-4} mols^{-1}.

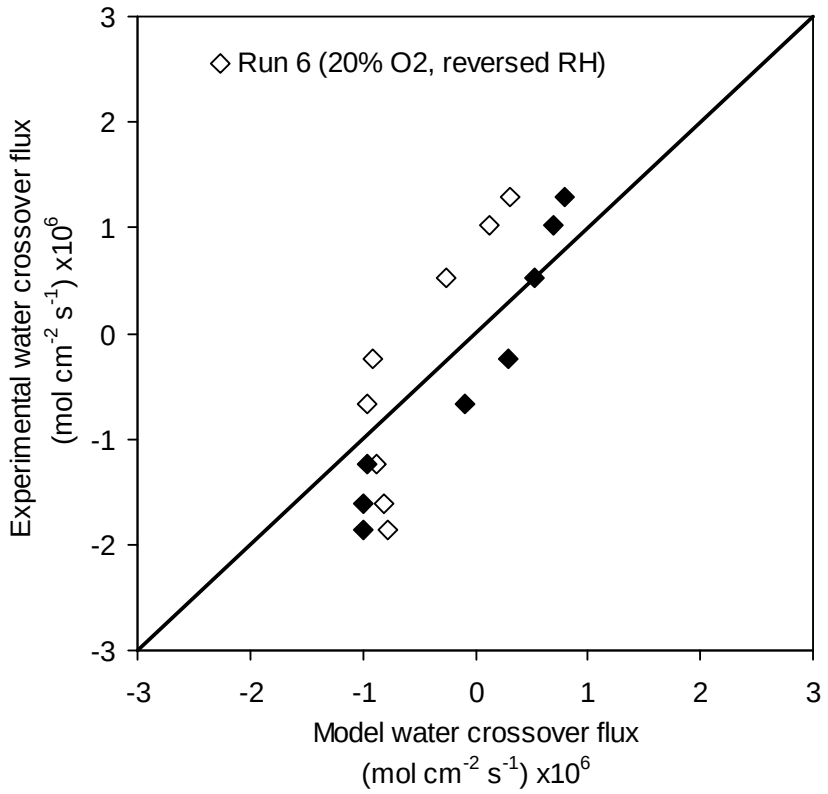

Figure 25. Comparison between experimental water crossover flux and model predictions on run 6 from 'best fit' values fitting run 1. Solid symbols: DRF results; hollow symbols: CDF results. T = 60 °C, P_A= 230 kPa, P_C = 200 kPa, $RH_{in,A}$ = 75%, $RH_{in,C}$ = 25%, H_2 flow rate = 3.13×10^{-3} mols^{-1}, N_2 flow rate = 2.98×10^{-3} mols^{-1}, O_2 flow rate = 7.46×10^{-4} mols^{-1}.

5.3. Roundup

Water crossover data have been applied for model validation and parameter estimation using the model developed by Berg et al. (2004). The observed residual deviation between calculated and measured water crossover fluxes at high current densities could be explained by a low maximum membrane water content, which would reduce the back diffusion of water to the anode. The decrease in effective oxygen diffusivity across the GDL with increasing oxygen concentration and water generation was likely a result of the presence of liquid water in the GDL. The fitted exchange current density was not well obtained due to the lack of data in the kinetic controlled regime. Effective resistance obtained at 20% oxygen concentration agreed well with Araki et al. (2005). When both current density and water crossover flux were used in the fitting process, more consistent

trends in the best fitted interfacial membrane water transfer coefficient were obtained. The overall product of the sum of square residuals (SSRs) in current density and water crossover flux was found to be an order of magnitude lower in DRF compared to CDF. The results show that the inclusion of water crossover in model validation and parameter fitting contributes to more reliable model parameter estimation.

6. Conclusions

The research project described in this thesis led to the following conclusions:

1) Through the combination of an infrared gas analyzer and an in-situ calibration system, a water crossover measurement equipment with high repeatability and high throughput was developed.

2) Water crossover in a running PEMFC was dominated by back diffusion in response to the increase in current densities, in a highly linear fashion. At high current densities diffusion effect ceased due to membrane saturation. Effects of inlet humidity was insignificant in changing the distribution of product water; while decreasing temperature and increasing cathode pressure led to higher RH gradient across the membrane downstream from the inlet and favoured more water transport to the anode, leading to higher voltage at the same load.

3) Adding a microporous layer to the cathode side of a PEMFC increased back diffusion of product water to the anode, but the effect diminished with increasing the cathode inlet humidity. Its effect on voltage was not as significant as feed humidification. The action of the microporous layer could be explained by an increased diffusional resistance to the cathode channel which forced produced water back to the anode, while a model based on capillary action gave unsatisfactory predictions to experimental results.

4) Water crossover data was found to be useful in evaluating PEMFC models. As a complement to polarization data for curve fitting, it provided more reliable parameter estimates with significantly lower overall residuals.

All the above results demonstrated the importance of experimental data in water crossover to studying both qualitatively and quantitatively the relationship between fuel cell configuration and operating conditions on the cell performance. Looking ahead, there could be some future work that could be done. The range of operating conditions for water crossover studies could be extended. One particularly interesting situation would be

the use of saturated feeds in the test. The saturation level of the membrane at maximum water vapour activity could be examined, and, if water crossover still decreases with increasing load, it would suggest the existence of Schroeder's paradox in the running fuel cell. Also the impact of liquid water generated may also be studied in terms of polarization and also water crossover. This may involve the observation of water concentration patterns against sampling time as an additional parameter of study. Another scenario is the operation at limiting current densities, so that water management can play a more significant role in reactant transfer processes. Also, other possible MEA structural changes such as membrane thickness, GDL coating and thickness could be studied which will bring a clearer picture to water transfer processes in a running PEMFC.

References

Adachi, M. Navessin, T. Xie, Z. Frisken, B. and Holdcroft, S. 2009. Correlation of In Situ and Ex Situ Measurements of Water Permeation Through Nafion NRE211 Proton Exchange Membranes. *J. Electrochem. Soc.* 156: B782-B790.

Araki, T. Koori, H. Taniuchi, T. and Onda, K. 2005. Simulation of the current density distribution for a PEMFC by using measured electrochemical and physical properties of the membrane. *J. Power Sources* 152: 60-66.

Atiyeh, H. Karan, K. Peppley, B. Phoenix, A. Halliop, E. and Pharoah, J. 2007. Experimental investigation of the role of a microporous layer on the water transport and performance of a PEM fuel cell. *J. Power Sources* 170: 111-121.

Auble, D.L. and Meyers, T.P. 1992. An open path, fast response infrared-absorption gas analyzer for H2O and CO2. *Bound.-Lay. Meteorol.* 59: 243-256.

Barbir, F. 2005. *PEM Fuel Cells: Theory and Practice*. Amsterdam: Academic Press.

Basu, S. Xu, H. Renfro, M.W. and Cetegen, B.M. 2006. In situ optical diagnostics for measurements of water vapor partial pressure in a PEM fuel cell. *J. Fuel Cell Sci. Technol.* 3: 1-7.

Basu, S. Renfro, M.W. and Cetegen, B.M. 2006. Spatially resolved optical measurements of water partial pressure and temperature in a PEM fuel cell under dynamic operating conditions. *J. Power Sources* 162: 286-293.

Beers, K. 2007. *Numerical methods for chemical engineering: applications in MATLAB*. New York: Cambridge University Press.

Bentley, R. 1998. *Temperature and Humidity Measurement*. Singapore: Springer.

Berg, P. Promislow, K. St Pierre, J. Stumper, J. and Wetton, B. 2004. Water management in PEM fuel cells. *J. Electrochem. Soc.* 151: A341-A353.

Bird, R. Stewart, W. and Lightfoot, E. 2007. *Transport Phenomona Revised 2nd Ed.* New York: John Wiley & Sons.

Buchi, F. and Srinivasan, S. 1997. Operating proton exchange membrane fuel cells without external humidification of the reactant gases - Fundamental aspects. *J. Electrochem. Soc.* 144: 2767-2772.

Buck, A. 1981. New equations for computing vapor pressure and enhancement factor. *J. Appl. Meteor.* 20: 1527-1532.

Cheng, X. Zhang, J. Tang, Y. Song, C. Shen, J. Song, D. et al. 2007. Hydrogen crossover in high-temperature PEM fuel cells. *J. Power Sources* 167: 25-31.

Choi, K. Peck, D. Kim, C. Shin, D. and Lee, T. 2000. Water transport in polymer membranes for PEMFC. *J. Power Sources* 86: 197-201.

Choi, P. Jalani, N.H. and Datta, R. 2005. Thermodynamics and proton transport in Nafion - II. Proton diffusion mechanisms and conductivity. *J. Electrochem. Soc.* 152: E123-E130.

Colinart, T. Chenu, A. Didierjean, S. Lottin, O. and Besse, S. 2009. Experimental study on water transport coefficient in Proton Exchange Membrane Fuel Cell. *J. Power Sources* 190: 230-240.

Chemical Rubber Company 2008. *CRC Handbook of Chemistry and Physics*. Cleveland, Ohio: CRC Press.

Dai, W. Wang, H. Yuan, X. Martin, J. Luo, Z. and Pan, M. 2008. Measurement of the water transport rate in a proton exchange membrane fuel cell and the influence of the gas diffusion layer. *J. Power Sources* 185: 1267-1271.

Dai, W. Wang, H. Yuan, X. Martin, J. Shen, J. Luo, Z. et al. 2009. Measurement of water transport rates across the gas diffusion layer in a proton exchange membrane fuel cell, and the influence of polytetrafluoroethylene content and micro-porous layer. *J. Power Sources* 188: 122-126.

Dean, J. 1995. *Analytical Chemistry Handbook*. New York: McGraw-Hill.

Dimitrova, P. Friedrich, K.A. Vogt, B. and Stimming, U. 2002. Transport properties of ionomer composite membranes for direct methanol fuel cells. *J. Electrochem. Soc.* 532: 75-83.

Dong, Q. Kull, J. and Mench, M. 2005. Real-time water distribution in a polymer electrolyte fuel cell. *J. Power Sources* 139: 106-114.

Endoh, E. Terazono, S. Widjaja, H. and Takimoto, Y. 2004. Degradation study of MEA for PEMFCs under low humidity conditions. *Electrochem. Solid State Lett.* 7: A209-A211.

Fraden, J. 2004. *Handbook of Modern Sensors - Physics, Designs and Applications*. New York: Springer.

Ge, S. Li, X. Yi, B. and Hsing, I. 2005. Absorption, desorption, and transport of water in polymer electrolyte membranes for fuel cells. *J. Electrochem. Soc.* 152: A1149-A1157.

Ge, S. Yi, B. and Ming, P. 2006. Experimental determination of electro-osmotic drag coefficient in Nafion membrane for fuel cells. *J. Electrochem. Soc.* 153: A1443-A1450.

Han, J. Park, G. Yoon, Y. Yang, T. Lee, W. and Kim, C. 2003. A new evaluation method of anode/cathode used for polymer electrolyte membrane fuel cell. *Int. J. Hydrogen Energy* 28: 609-613.

Hinds, G. Stevens, M. Wilkinson, J. de Podesta, M. and Bell, S. 2009. Novel in situ measurements of relative humidity in a polymer electrolyte membrane fuel cell. *J. Power Sources* 186: 52-57.

Husar, A. Higier, A. and Liu, H. 2008. In situ measurements of water transfer due to different mechanisms in a proton exchange membrane fuel cell. *J. Power Sources* 183: 240-246.

Ito, H. 1987. Balanced Adsorption Quartz Hygrometer. *IEEE Trans. Ultrason. Ferroelectr. Freq. Control* UFFC-34: 136-141.

Janssen, G. and Overvelde, M. 2001. Water transport in the proton-exchange-membrane fuel cell: Measurements of the effective drag coefficient. *J. Power Sources* 101: 117-125.

Ju, H. and Wang, C. 2004. Experimental validation of a PEM fuel cell model by current distribution data. *J. Electrochem. Soc.* 151: A1954-A1960.

Jung, S.H. Kim, S.L. Kim, M.S. Park, Y. and Lim, T.W. 2007. Experimental study of gas humidification with injectors for automotive PEM fuel cell systems. *J. Power Sources* 170: 324-333.

Jury, S. Pollock, M. and Mattern, J. 1972. The Activated Calcium Sulfate- Water Vapor Sorption Therm. *AIChE Journal* 18: 48-51.

Kim, S. and Mench, M.M. 2009. Investigation of temperature-driven water transport in polymer electrolyte fuel cell: Thermo-osmosis in membranes. *J. Membr. Sci.* 328: 113-120.

Kim, T. Lee, S. and Park, H. 2010. A study of water transport as a function of the micro-porous layer arrangement in PEMFCs. *Int. J. Hydrogen Energy* 35: 8631-8643.

Knights, S.D. Colbow, K.M. St-Pierre, J. and Wilkinson, D.P. 2004. Aging mechanisms and lifetime of PEFC and DMFC. *J. Power Sources* 127: 127-134.

Kocha, S. Yang, J. and Yi, J. 2006. Characterization of gas crossover and its implications in PEM fuel cells. *AIChE Journal* 52: 1916-1925.

Larminie, J. and Dicks, A. 2003. *Fuel Cell Systems Explained 2nd Ed.* West Sussex: John Wiley & Sons.

Liu, F. Lu, G. and Wang, C. 2007. Water transport coefficient distribution through the membrane in a polymer electrolyte fuel cell. *J. Membr. Sci.* 287: 126-131.

Lu, G. Liu, F. and Wang, C. 2007. An approach to measuring spatially resolved water crossover coefficient in a polymer electrolyte fuel cell. *J. Power Sources* 164: 134-140.

Majsztrik, P. Satterfield, M. Bocarsly, A. and Benziger, J. 2007. Water sorption, desorption and transport in Nafion membranes. *J. Membr. Sci.* 301: 93-106.

Majsztrik, P. Bocarsly, A. and Benziger, J. 2008. Water Permeation through Nafion Membranes: The Role of Water Activity. *J. Phys. Chem. B* 112: 16280-16289.

Mench, M. Dong, Q. and Wang, C. 2003a. In situ water distribution measurements in a polymer electrolyte fuel cell. *J. Power Sources* 124: 90-98.

Mench, M. Wang, C. and Ishikawa, M. 2003b. In situ current distribution measurements in polymer electrolyte fuel cells. *J. Electrochem. Soc.* 150: A1052-A1059.

Min, C. He, Y. Liu, X. Yin, B. Jiang, W. and Tao, W. 2006. Parameter sensitivity examination and discussion of PEM fuel cell simulation model validation Part II: Results of sensitivity analysis and validation of the model. *J. Power Sources* 160: 374-385.

Monroe, C. Romero, T. Merida, W. and Eikerling, M. 2008. A vaporization-exchange model for water sorption and flux in Nafion. *J. Membr. Sci.* 324: 1-6.

Motupally, S. Becker, A. and Weidner, J. 2000. Diffusion of water in Nafion 115 membranes. *J. Electrochem. Soc.* 147: 3171-3177.

Murahashi, T. Naiki, M. and Nishiyama, E. 2006. Water transport in the proton exchange-membrane fuel cell: Comparison of model computation and measurements of effective drag. *J. Power Sources* 162: 1130-1136.

Nishikawa, H. Kurihara, R. Sukemori, S. Sugawara, T. Kobayasi, H. Abe, S. et al. 2006. Measurements of humidity and current distribution in a PEFC. *J. Power Sources* 155: 213-218.

O'Hayre, R. Cha, S. Colella, W. and Prinz, F. 2006. *Fuel Cell Fundamentals*. New York: John Wiley & Sons.

Onishi, L.M. Prausnitz, J.M. and Newman, J. 2007. Water-nafion equilibria. Absence of Schroeder's paradox. *J. Phys. Chem. B* 111: 10166-10173.

Owejan, J.P. Owejan, J.E. Gu, W.B. Trabold, T.A. Tighe, T.W. and Mathias, M.F. 2010. Water Transport Mechanisms in PEMFC Gas Diffusion Layers. *J. Electrochem. Soc.* 157: B1456-B1464.

Oxby, P. *Multivariate weighted least squares as a preferable alternative to the determinant criterion for multiresponse parameter estimation*. PhD Thesis, University of Waterloo, Waterloo, ON, Canada. 1997.

Park, S. Lee, J.W. and Popov, B.N. 2006. Effect of carbon loading in microporous layer on PEM fuel cell performance. *J. Power Sources* 163: 357-363.

Pasaogullari, U. and Wang, C. 2004. Liquid water transport in gas diffusion layer of polymer electrolyte fuel cells. *Journal of the Electrochemcial Society* 151: A399-A406.

Perry, R. and Green, D. 2008. *Perry's Chemical Engineers' Handbook*. New York: McGraw-Hill.

Poling, B. Prausnitz, J. and O'Connor, J. 2007. *The Properties of Gases and Liquids*. New York: McGraw-Hill.

Rajalakshmi, N. Jayanth, T.T. Thangamuthu, R. Sasikumar, G. Sridhar, P. and Dhathathreyan, K.S. 2004. Water transport characteristics of polymer electrolyte membrane fuel cell. *Int. J. Hydrogen Energy* 29: 1009-1014.

Sauriol, P. Nobes, D. Bi, X. Stumper, J. Jones, D. and Kiel, D. 2009. Design and Validation of a Water Transfer Factor Measurement Apparatus for Proton Exchange Membrane Fuel Cells. *J. Fuel Cell Sci. Technol.* 6: 041014.

Sparks, D. Smith, R. Massoud-Ansari, S. and Najafi, N. Coriolis mass flow, density and temperature sensing with a single vacuum sealed MEMS chip. In *Solid-State Sensor, Actuator and Microsystems Workshop*. Hilton Head Island, South Carolina: 2004:

Springer, T. Zawodzinski, T. and Gottesfeld, S. 1991. Polymer Electrolyte Fuel-Cell Model. *J. Electrochem. Soc.* 138: 2334-2342.

Stumper, J. Campbell, S. Wilkinson, D. Johnson, M. and Davis, M. 1998. In-situ methods for the determination of current distributions in PEM fuel cells. *Electrochim. Acta* 43: 3773-3783.

Stumper, J. Haas, H. and Granados, A. 2005. In situ determination of MEA resistance and electrode diffusivity of a fuel cell. *Journal of the Electrochemcial Society* 152: A837-A844.

Sur, R. Boucher, T.J. Renfro, M.W. and Cetegen, B.M. 2010. In Situ Measurements of Water Vapor Partial Pressure and Temperature Dynamics in a PEM Fuel Cell. *J. Electrochem. Soc.* 157: B45-B53.

Tao, W. Min, C. Liu, X. He, Y. Yin, B. and Jiang, W. 2006. Parameter sensitivity examination and discussion of PEM fuel cell simulation model validation Part I.

Current status of modeling research and model development. *J. Power Sources* 160: 359-373.

Watanabe, M. Uchida, H. and Emori, M. 1998. Polymer electrolyte membranes incorporated with nanometer-size particles of Pt and/or metal-oxides: Experimental analysis of the self-humidification and suppression of gas-crossover in fuel cells. *J. Phys. Chem. B* 102: 3129-3137.

Weber, A. and Newman, J. 2005. Effects of microporous layers in polymer electrolyte fuel cells. *J. Electrochem. Soc.* 152: A677-A688.

Wijmans, J.G. and Baker, R.W. 1995. The solution-diffusion model- a review. *J. Membr. Sci.* 107: 1-21.

Wilson, J. 2005. *Sensor Technology Handbook* . Boston: Elsevier.

Wu, J.F. Yuan, X.Z. Wang, H.J. Blanco, M. Martin, J.J. and Zhang, J.J. 2008. Diagnostic tools in PEM fuel cell research: Part II - Physical/chemical methods. *Int. J. Hydrogen Energy* 33: 1747-1757.

Yan, Q. Toghiani, H. and Wu, J. 2006. Investigation of water transport through membrane in a PEM fuel cell by water balance experiments. *J. Power Sources* 158: 316-325.

Ye, X. and Wang, C. 2007a. Measurement of water transport properties through membrane-electrode assemblies. *J. Electrochem. Soc.* 154: B676-B682.

Ye, X. and Wang, C. 2007b. Measurement of water transport properties through membrane electrode assemblies - Part II. Cathode diffusion media. *J. Electrochem. Soc.* 154: B683-B686.

Zawodzinski, T.A. Neeman, M. Sillerud, L. and Gottesfeld, S. 1991. Determination of Water Diffusion Coefficients in Perfluorosulfonate Ionomeric Membranes. J. Phys. Chem. 95: 6040-6044.

Zawodzinski, T. Springer, T. Davey, J. Jestel, R. Lopez, C. Valerio, J. et al. 1993a. A comparative study of water updake by and transport through ionomeric fuell cell membranes. *J. Electrochem. Soc.* 140: 1981-1985.

Zawodzinski, T. Derouin, C. Radzinski, S. Sherman, R. Smith, V. Springer, T. et al. 1993b. Water uptake by and transport through Nafion(R) 117 membranes. *J. Electrochem. Soc.* 140: 1041-1047.

Zawodzinski, T. Davey, J. Valerio, J. and Gottesfeld, S. 1995. The water-content dependence of electroosmotic drag in proton-conducting polymer electrolytes. *Electrochim. Acta* 40: 297-302.

Appendices

Confidence Intervals for Parameter Estimation

For CDF, the estimate for the *j*-th element in the parameter vector θ is given by (Beers 2007)

$$\widehat{\theta}_j \pm \frac{\sum_i \left(\Delta \overline{I}_i\right)^2}{N-4} t_{N-4,0.05} \sqrt{\left\{\left(V^T V\right)^{-1}\right\}_{jj}} \qquad [38]$$

where $t_{v,\frac{\alpha}{2}}$ is the two tailed student *t* value with degree of freedom *v* and $\alpha/2$ probability.

The elements of *V* are given by

$$V_{i,j} = \frac{\partial\left(\Delta \overline{I}_i\right)}{\partial \theta_j} \qquad [39]$$

For DRF, the estimate is (Oxby 1997)

$$\widehat{\theta}_j \pm t_{N-4,0.05} \sqrt{\left\{\Sigma\right\}_{jj}} \qquad [40]$$

where

$$\Sigma = \left(X^T W X\right)^{-1} X^T W \Sigma_\varepsilon W X \left(X^T W X\right)^{-1} \qquad [41]$$

$$\begin{pmatrix} X_{2i-1,j} \\ X_{2i,j} \end{pmatrix} = \begin{pmatrix} \frac{\partial\left(\Delta \overline{I}_i\right)}{\partial \theta_j} \\ \frac{\partial\left(\Delta \overline{J}_{H_2O,i}\right)}{\partial \theta_j} \end{pmatrix} \qquad [42]$$

$$W = I_N \otimes \frac{1}{N} \begin{pmatrix} \sum_i \left(\Delta \overline{I}_i\right)^2 & 0 \\ 0 & \sum_i \left(\Delta \overline{J}_{H_2O,i}\right)^2 \end{pmatrix}^{-1} \qquad [43]$$

$$\Sigma_{\varepsilon} = I_N \otimes \frac{1}{N - 4/2} \begin{pmatrix} \sum_i \left(\Delta \overline{I_i}\right)^2 & \sum_i \left(\Delta \overline{I_i}\right)\left(\Delta \overline{J}_{H_2O,i}\right) \\ \sum_i \left(\Delta \overline{I_i}\right)\left(\Delta \overline{J}_{H_2O,i}\right) & \sum_i \left(\Delta \overline{J}_{H_2O,i}\right)^2 \end{pmatrix} \quad [44]$$

where I_N is the N by N identity matrix.

MATLAB Code for the Berg Model

Below is a MATLAB code that runs the Berg model.

```
% This program uses the ode45 to calculate and fit the current density and
% water crossover rate

% Prefix I indicates an integrated (or global) quantity by ODE
% Prefix d indicates a differential (or local) quantity in ODE
% Overall water crossover Jwt (sum of EOD and back diffusion)
% Anode water molar flowrate                                          Qa2
% Cathode water molar flowrate                                        Qc2
% Conductivity                                                        sigma
% Current density                                                     I
% Temperature                                                         T
% Hydrogen molar flowrate                                             Qa1
% Oxygen molar flowrate                                               Qc1
% Nitrogen molar flowrate                                             Qc3
% Anode pressure                                                      Pa
% Cathode pressure                                                    Pc
% Voltage                                                             U
% ODE data structure   du=[Jwt dQa2 dQc2 sigma I dT dQa1 dQc1 dQc3 dPa dPc dU]
%                       u=[IJwt Qa2 Qc2 Isigma II T Qa1 Qc1 Qc3 Pa Pc U]


% Membrane interfacial water transfer coefficient    gamma
% Oxygen diffusivity factor                                           delta
% Exchange current density                                            ioc
% Effective membrane conductivity                                     sigma
% The four parameters above are in the 'log' form for easy manipulation
% For the actual value of the parameter gamma would be
% actual value = value reported in Berg et al. * (5 ^ gamma)
% fitting parameter           parameters=[gamma delta ioc sigma]
% fitting parameter    fp=[gamma delta ioc]
% fitting parameter    sigma
% Sulfonic acid group concentration                                   a
% Water diffusion coefficient                                         dw
% Proton diffusion coefficient                                        dplus
% Ion exchange equilibrium constant                                   K0
% Enthalpy of hydronium formation                                     H0
% Henry's constant for oxygen                                         Ho
% Membrane thickness                                                  Lm
% Activation energy for water diffusion                               Ea
% Cathode oxygen reference concentration                              Coref
% Cathode electrochemical transfer coefficient                        alphac
% Open circuit potential                                              E0
% Channel width                                                       Lw
% Ideal gas constant                                                  R
% Faraday's constant                                                  F
% system parameter            sp=[a dw dplus K0 H0 Ho Lm Ea Coref alphac E0 Lw]
% universal constants uc=[R F]


% Experimental voltage                                                U
% Experimental current density                                        I_stoic
% Experimental water crossover rate                                   Jw_stoic
% Data point range for fitting                                        partial
% Model accepts voltage as input and gives the following
% Model current density                                               I_model
% Model water crossover rate                                          Jw_model
% Choice of ODE solver to integrate data structure u along x
```

```
function [I_model,Jw_model]=ode_solve_IJw_manual(parameters,U,I_stoic,Jw_stoic,partial)

%set universal constants
R=8.3145;
F=96500;
uc=[R F];

%set system paramters
a=1200;
dw=2.1e-7;
dplus=1.6e-8;
K0=6.2;
H0=-52300;
Ho=2e5*101325*1e-6; %convert to atm cm3/mol to Pa m3/mol
Lm=25e-6;
Ea=2436;
Coref=9.6;
alphac=1;
E0=0.95; % read from fig 3 of Berg
Lw=1e-3;

%channel length
Lc=0.67/6;
%number of channels
N=36;
%Cell active area
Area=Lw*Lc*N;

%set inlet values u0
slpm2mol_s=101325*0.001/(R*273.15*60);

Pa0=230000;
Pc0=230000;
T0=343.15;

% number of data points n_pt
n_pt=length(U);

%initialize I_model and Jw_model and utilization
I_model=zeros(1,n_pt);
Jw_model=zeros(1,n_pt);
utilization=zeros(1,n_pt);

% Enter inlet material rates here
% A column vector has to be created with each element corresponding to the condition
% for each point on the polarization curve
% Below is an example of having different cathode water flow rates from points
% 1-7, 8-14, 15-21 and 22-28. The flow rate was transformed to a column vector.

Qa10=6*7.44e-4/N*ones(n_pt,1);
Qa20=544/60/18036/N*ones(n_pt,1);
Qc10=5*.21*7.44e-4/N*ones(n_pt,1);
Qc30=5*.79*7.44e-4/N*ones(n_pt,1);
temp_Qc20=ones(7,1)*[141 454 141 454]/60/18036/N;
Qc20=temp_Qc20(:);

% convert all parameters
sigma0=106723*(5^parameters(4));
delta0=8.99E-4*(5^parameters(2));
gamma0=5.7E-6*(5^parameters(1));
ioc0=425.721944184939*(5^parameters(3));

II0=1e-8; % a pseudo zero
Isigma0=1e-8; % a pseudo zero
IJwt0=1e-8; % a pseudo zero

%solve for dplus to fit desired sigma0 at saturation
%at saturation, Cw=14 for all y so an integration procedure is reduced to
%simple algebric equation
Ke=K0*exp(-H0/R*(1/T0-1/298));
Cw=14;
Cplus=-Ke*Cw/2+sqrt((Ke*Cw/2)^2+Ke*Cw);
dplus=sigma0*R*T0*Lm/a/F^2/Cplus/exp(-1683/T0)/Cw;

fp0=[gamma0 delta0 ioc0];
sp=[a dw dplus K0 H0 Ho Lm Ea Coref alphac E0 Lw];

% initialization of model outputs
I_model=zeros(n_pt,1);
Jw_model=zeros(n_pt,1);
```

```
%calculation along channel by ode
for i=1:n_pt
    if ismember(i,partial) %start if it is in the partial array
        u0=[IJwt0 Qa20(i) Qc20(i) Isigma0 II0 T0 Qa10(i) Qc10(i) Qc30(i) Pa0 Pc0];
         try
         [t,u]=ode15s(@(x,u)differential_short(x,u,fp0,sp,U(i),uc,I_stoic(i)),[0,Lc],u0);
        catch
         t=[0 Lc]; u=vertcat(u0,u0); %no solution for I at that point
        end
        I_model(i)=u(end,5)/Lc;
        Jw_model(i)=u(end,1)*Lw*N;

    end
end
end
```

```
% This is the 1D model called by the ODE function

function du=differential(x,u,fp,sp,U,uc,I_stoic)

% assign variables with names for the sake of readability
IJwt=u(1); Qa2=u(2); Qc2=u(3); Isigma=u(4); II=u(5); T=u(6); Qa1=u(7); Qc1=u(8);
Qc3=u(9); Pa=u(10); Pc=u(11);
gamma=fp(1); delta=fp(2); ioc=fp(3);
a=sp(1); dw=sp(2); dplus=sp(3); K0=sp(4); H0=sp(5); Ho=sp(6); Lm=sp(7); Ea=sp(8);
Coref=sp(9); alphac=sp(10); E0=sp(11); Lw=sp(12);
R=uc(1); F=uc(2);

% isothermal and isobaric conditions
dT=0;
dPa=0;
dPc=0;

% Antoine eqn, T in deg C, Psat in Pa
Psat=10^(8.07131-1730.63/(T-273.15+233.426))/760*101325;

% cathode
Cc2=Pc/R/T*Qc2/(Qc1+Qc2+Qc3);
Pc2=Pc*Qc2/(Qc1+Qc2+Qc3);
if (Pc2>Psat) %over saturation
   Pc2=Psat;
   Cc1=(Pc-Psat)/R/T*Qc1/(Qc1+Qc3);
   Cc3=(Pc-Psat)/R/T*Qc3/(Qc1+Qc3);
else %under saturation
   Cc1=Pc/R/T*Qc1/(Qc1+Qc2+Qc3);
   Cc3=Pc/R/T*Qc3/(Qc1+Qc2+Qc3);
end
% anode
Ca2=Pa/R/T*Qa2/(Qa1+Qc2);
Pa2=Pa*Qa2/(Qa1+Qc2);
if (Pa2>Psat) %over saturation
   Pa2=Psat;
   Ca1=(Pa-Psat)/R/T*Qa1/(Qa1+Qa2);
else %under saturation
   Ca1=Pa/R/T*Qa1/(Qa1+Qa2);
end

% calculation of water activity
awa=Pa2/Psat;
awc=Pc2/Psat;

% calculation of Cwa_star, Cwc_star using equation 29
if (awa<1)
   Cwa_star=0.043+17.81*awa-39.85*awa^2+36*awa^3;
else
   Cwa_star=14;
end
if (awc<1)
   Cwc_star=0.043+17.81*awc-39.85*awc^2+36*awc^3;
else
   Cwc_star=14;
end

% largest current bound such that U(cal)<U
% U(cal)=E0-R*T/alphac/F*log(Coref*Ho/ioc/R/T*I/(Cc1-delta*I))-I/sigma-
R*T/F*log(Caplus/Ccplus)
%      <E0-R*T/alphac/F*log(Coref*Ho/ioc/R/T*I/(Cc1-delta*I))-R*T/F*log(Caplus/Ccplus)
%      <E0-R*T/alphac/F*log(Coref*Ho/ioc/R/T*I/(Cc1-delta*I))+0.1 ...(*),
%      -R*T/F*log(Caplus/Ccplus)<=0.07685 for 0.043<=Cw<=14, 273<=T<=373
%      sigma<sigma_sat for 0.043<=Cw<=14, 273<=T<=373
% Equate (*) with U and solve for I
% At saturation,
%   Cwa=(-M2+sqrt(M2^2-4*M1*M3))/2/M1;
%      where
%      M1=a*dw*exp(-Ea/T)/2/Lm;
%       M2=a*gamma;
%       M3=I/F-a*gamma*Cwa_star-a*dw*exp(-Ea/T)/2/Lm*Cwc^2;
%      Cwc=14;
%   To have +ve Cwa we have M3<0, we equate M3 with -1/F (a small number)

temp_pp=[Cwc_star Cwa_star T Cc1];
Ke=K0*exp(-H0/R*(1/T-1/298));
Cwc=14;
ubI1=F*(-1/F+a*gamma*Cwa_star+a*dw*exp(-Ea/T)/2/Lm*Cwc^2);
%I< ubI1 to ensure Cwa>0 at saturation
ubI2=Cc1/((Coref*Ho/ioc/R/T)/exp((E0-U+0.1)/(R*T/alphac/F))+delta);
% I>ubI2 to ensure U(cal)<U
```

```
% ensure both inequalities to be valid

% solve for local current density given conditions and voltage
try
[I,fval]=fzero(@(I)cal_error_in_I(I,temp_pp,fp,sp,U,uc),[1 ubI1]);
catch
[I,fval]=fzero(@(I)cal_error_in_I(I,temp_pp,fp,sp,U,uc),[1 ubI2]);
end

% calculation of Cwa, Cwc using equations 41-44
xi_plus=Cwc_star+Cwa_star+I/(2*gamma*a*F);
xi_minus=(Cwc_star-Cwa_star+5*I/(2*gamma*a*F))/(1+dw*exp(-Ea/T)*xi_plus/Lm/gamma);
Cwc=1/2*(xi_plus+xi_minus);
Cwa=1/2*(xi_plus-xi_minus);
if Cwc>14
        Cwc=14;
        M1=a*dw*exp(-Ea/T)/2/Lm;
        M2=a*gamma;
        M3=I/F-a*gamma*Cwa_star-a*dw*exp(-Ea/T)/2/Lm*Cwc^2;
        Cwa=max(roots([M1 M2 M3]));
end

% calculation of Jw using equation 40
Jw=a*dw*exp(-Ea/T)*(Cwa^2-Cwc^2)/2/Lm;

% calculation of sigma by integration

temp_p=[Jw a dw Ea T dplus Ke Cwa];
sigma = 1/(R*T/a/F^2*quadl(@(y)cal_dsigma(y,temp_p),0,Lm));

% differential flow rates
Jwt=Jw+I/F;
dQa1=-I/2/F*Lw;
dQa2=-Jwt*Lw;
dQc1=-I/4/F*Lw;
dQc2=(Jwt+I/2/F)*Lw;
dQc3=0;


% output du
du=[Jwt dQa2 dQc2 sigma I dT dQa1 dQc1 dQc3 dPa dPc]';

end
```

```
% This is the equation to be solved by fzero in the 1-D model
function error_in_I=cal_error_in_I(I,temp_pp,fp,sp,U,uc)
%load parameters
Cwc_star=temp_pp(1);
Cwa_star=temp_pp(2);
T=temp_pp(3);
Cc1=temp_pp(4);
gamma=fp(1); delta=fp(2); ioc=fp(3);
a=sp(1); dw=sp(2); dplus=sp(3); K0=sp(4); H0=sp(5); Ho=sp(6); Lm=sp(7); Ea=sp(8);
Coref=sp(9); alphac=sp(10); E0=sp(11); Lw=sp(12);
R=uc(1); F=uc(2);


% calculation of Cwa, Cwc using equations 41-44
xi_plus=Cwc_star+Cwa_star+I/(2*gamma*a*F);
xi_minus=(Cwc_star-Cwa_star+5*I/(2*gamma*a*F))/(1+dw*exp(-Ea/T)*xi_plus/Lm/gamma);
Cwc=1/2*(xi_plus+xi_minus);
Cwa=1/2*(xi_plus-xi_minus);
if Cwc>14
   Cwc=14;
        M1=a*dw*exp(-Ea/T)/2/Lm;
        M2=a*gamma;
        M3=I/F-a*gamma*Cwa_star-a*dw*exp(-Ea/T)/2/Lm*Cwc^2;
        Cwa=max(roots([M1 M2 M3]));
end

% calculation of Jw using equation 40
Jw=a*dw*exp(-Ea/T)*(Cwa^2-Cwc^2)/2/Lm;

% calculation of sigma by integration
Ke=K0*exp(-H0/R*(1/T-1/298));
temp_p=[Jw a dw Ea T dplus Ke Cwa];
sigma = 1/(R*T/a/F^2*quadl(@(y)cal_dsigma(y,temp_p),0,Lm));

% calculation of error in I using equation 49
Caplus=-Ke*Cwa/2+sqrt((Ke*Cwa/2)^2+Ke*Cwa);
Ccplus=-Ke*Cwc/2+sqrt((Ke*Cwc/2)^2+Ke*Cwc);
error_in_I=(U-(E0-R*T/alphac/F*log(Coref*Ho/ioc/R/T*I/(Cc1-delta*I))-
(I/sigma+R*T/F*log(Caplus/Ccplus))));

end



%%%%%%%%%%%%%%%%%%%%%%%%%%%%%%%%%%%%%%%%%%%%%%%%%%%%%%%%%%%%%%%%%%%%%%%%%%%
function dsigma=cal_dsigma(y,temp_p)
%load parameters
Jw=temp_p(1); a=temp_p(2); dw=temp_p(3); Ea=temp_p(4); T=temp_p(5); dplus=temp_p(6);
Ke=temp_p(7); Cwa=temp_p(8);

%by solving eqn 22 and 24
Cw=sqrt(2*(-Jw*y/a/dw/exp(-Ea/T)+Cwa^2/2));

%eqn 23
Dplus=dplus*exp(-1683/T)*Cw;
%eqn 20
Cplus=-Ke*Cw/2+sqrt((Ke*Cw/2).^2+Ke*Cw);
%eqn 48
dsigma=1./(Dplus.*Cplus);

end
```